MODELING REVEALS CORTICAL DYNEIN-DEPENDENT OSCILLATIONS IN BIPOLAR SPINDLE LENGTH

A PREPRINT

Dayna Mercadante
Bioinformatics and Computational Biology Program
Worcester Polytechnic Institute
Worcester, MA 01609 USA
damercadante@wpi.edu

Amity Manning
Department of Biology and Biotechnology
Worcester Polytechnic Institute
Worcester, MA 01609 USA
almanning@wpi.edu

Sarah Olson
Department of Mathematical Sciences
Worcester Polytechnic Institute
Worcester, MA 01609 USA
sdolson@wpi.edu

August 4, 2020

ABSTRACT

Proper formation and maintenance of the mitotic spindle is required for faithful cell division. While much work has been done to understand the roles of the key force components of the mitotic spindle, identifying the consequences of force perturbations in the spindle remains a challenge. We develop a computational framework accounting for the minimal force requirements of mitotic progression. To reflect early spindle formation, we account for microtubule dynamics and interactions with major force-generating motors, excluding chromosome interactions that dominate later in mitosis. We directly integrate our experimental data to define and validate the model, and then use simulations to analyze individual force components over time and their relationship to spindle dynamics, making it distinct from previously published models. Rather than achieving and maintaining a constant bipolar spindle length, oscillations in pole to pole distance occur that coincide with microtubule binding and force generation by cortical dynein. In the context of high kinesin-14 (HSET) activity, we identify the requirement of high cortical dynein activity for bipolar spindle formation.

Introduction

Mathematical and computational modeling of biological processes can bypass experimental limitations and provide a framework to identify and manipulate individual molecular components. An appealing candidate for such modeling is the process of cell division [1], which involves formation of the mitotic spindle to organize and separate the genetic material of a cell into two identical daughter cells. The assembly of the mitotic spindle is initiated by the nucleation of microtubules (MTs) at an organelle known as the centrosome [2]. Normal mitotic cells have two centrosomes (spindle poles) and they are positioned in response to mechanical forces, primarily driven by the activity of motor proteins [3, 4, 5, 6, 7]. As mitosis proceeds, the mitotic spindle forms and maintains a bipolar configuration, with the two centrosomes positioned at opposite sides of the cell.

Many models have been developed to understand early centrosome separation and spindle formation [8, 9, 10, 11, 12, 13, 14, 15], chromosome dynamics, [16, 17, 18, 19, 20, 21], and spindle elongation during anaphase [22, 23, 24]. Since the exact spatiotemporal motor force generation is not known, computational force-balance models have been used to understand key mechanistic components that modulate positioning of spindle poles and bipolar spindle formation [25, 26, 27, 13, 28]. Due to the large number of motor interactions [29, 6, 30], computational models generally simplify dynamics and focus on the role of a limited number of MT-motor interactions. Additionally, since many modeling

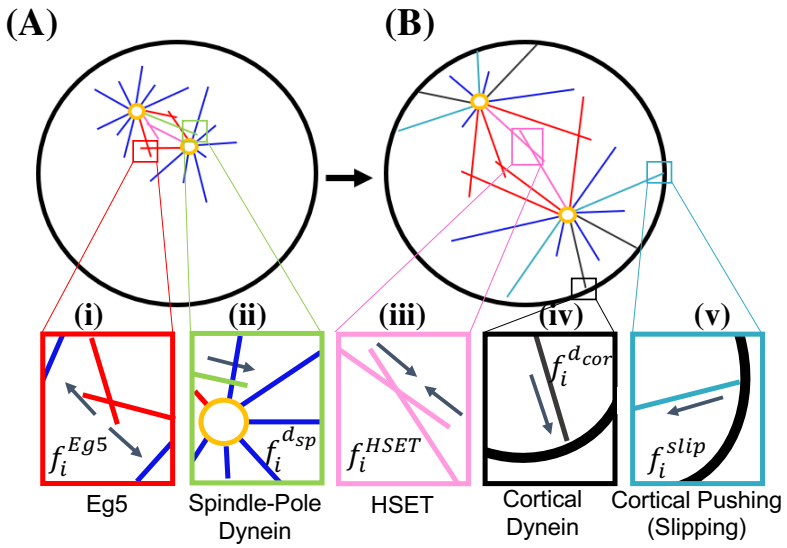

Figure 1: **MT-associated forces are involved in forming and maintaining a bipolar spindle in the absence of chromosome interactions**. A balance of pushing and pulling forces are required for proper centrosome separation in (A) and maintenance of spindle bipolarity in (B). (i) Eg5 pushes centrosomes apart by generating force at antiparallel MT overlap regions. (ii) Dynein localized to spindle poles binds to and pulls MTs from the opposing spindle pole. (iii) HSET pulls centrosomes together by generating force at antiparallel MT overlap regions. (iv) Dynein localized to the cell cortex bound to MTs pulls the centrosome towards the boundary. (v) MTs growing and slipping against the cell cortex push the centrosome away from the boundary.

studies and experimental parameters are based on those of embryos or yeast [31, 18, 10, 32], biological interpretation and application to mammalian cells, with a more complex spindle and genome, is challenging.

Proper formation of the mitotic spindle is required for accurate chromosome segregation, and while the molecular regulation of segregation onset is dependent on stable MT attachments to chromosomes [33], chromosomes are dispensable for bipolar spindle assembly [34, 35, 36]. Hence, we develop a minimal computational model to analyze centrosome movement and mammalian mitotic spindle formation in the absence of chromosomes, directly integrating live-cell imaging with model simulation. Analysis of individual force components over time makes this model distinct from previously published models that do not explore time-dependent changes in forces or their relationship to spindle dynamics.

To better understand the key mechanistic requirements of bipolar spindle formation and maintenance, we study the role of forces driving centrosome movement by stochastic MT interactions with three motor proteins: kinesin-5 (Eg5), kinesin-14 (HSET), and dynein. Centrosome movement and bipolar spindle formation for both simulations and experimental data are on the same time scale and further simulations of motor-perturbations led to altered final spindle lengths. Results from the model indicate that dynein at the cell cortex antagonizes HSET activity to directly impact bipolar spindle length and promote oscillations in pole to pole distance. Since centrosome and spindle pole positioning is implicated in chromosome attachments and alignment [37, 38, 39], our model suggests that cortical dynein-dependent regulation of spindle length promotes proper chromosome attachments and segregation, particularly in cancer contexts where HSET activity is high.

Materials and Methods

Model Overview

In our two-dimensional simulations, the cell cortex is a rigid, circular boundary, with a diameter of 30 μm, capturing a mammalian cell that has rounded as it enters mitosis [40, 41, 42]. We consider MT-motor protein derived forces that are responsible for centrosome movement and bipolar spindle formation. Where available, experimentally defined parameters using mammalian cell culture were chosen from the literature, and all parameters described below are listed in Table S1 in the Supporting Material. The model is benchmarked on previous *in vitro* assays and modeling

approaches that capture dynamic centrosome positioning and cell division [43, 44, 27, 13]. Additional model validation and details are provided in the Supporting Material.

Dynamic Microtubules

MTs are elastic filaments oriented such that their plus-ends, those that dynamically grow and shrink [45], point outward while their minus ends remain anchored at the centrosome [46, 47, 48] (Fig. 1). We consider MT minus-ends to remain embedded in the centrosome, to account for crosslinkers that maintain spindle-pole focusing throughout mitosis [49, 50]. MT plus-ends undergo dynamic instability [45], meaning that they are stochastically switching between states of growing (at a velocity v_g) and shrinking (at a velocity v_s if not bound to motor proteins and v_b if bound to cortical dynein). Each MT is characterized by a unit direction vector $\vec{m}$, has a length ℓ, and is nucleated from one of the two centrosomes.

Cortical Forces

Dynein is a minus-end directed motor that is localized at the cell cortex (cor) where it binds to MT plus-ends and pulls centrosomes towards the boundary of the cell [51, 9, 52, 43, 44, 53, 54], as illustrated in Fig. 1 iv. We assume that MTs can either be pulled towards the cell cortex by binding to dynein or push and slip against the cell cortex when binding does not occur. Cortical dynein is assumed to be uniformly distributed along the boundary and each MT within a distance $\mathcal{D}_{d_{cor}}$ to the boundary has a probability P_d of binding to dynein. Following a standard Monte Carlo Method, we choose n_d from a uniform distribution, $n_d \in \mathcal{U}[0,1]$, and binding to dynein will occur if $n_d \leq P_d$. The pulling force generated by cortical dynein on the i^{th} MT nucleated from the c^{th} centrosome follows a standard linear force-velocity relationship [55]:

$$f_i^{d_{cor}} = f_{0,d}\left(1 - \frac{v_{i,d}}{v_{0,d}}\right), \tag{1}$$

where $f_{0,d}$ is the stall force of dynein, $v_{0,d}$ is the walking velocity of dynein, and $v_{i,d}$ is defined as the difference between the magnitude of the centrosome velocity and the poleward flux (v_f) of the MT. The total pulling force by cortical dynein on the c^{th} centrosome is then:

$$\vec{F}_c = \sum_{i=1}^{N_{c,d_{cor}}} -f_i^{d_{cor}} \exp\left(-\frac{\ell_i}{K d_{cor}}\right)\vec{m}_i, \tag{2}$$

where $N_{c,d_{cor}}$ is the total number of MTs on centrosome c that bind to cortical dynein, K is a scaling factor, and d_{cor} is the minimum distance from the centrosome to the cell cortex. The force acting on the centrosome from a MT bound to dynein decreases exponentially with increased MT length [56], and we use this for every MT-motor interaction considered in this model. MTs will stay bound to cortical dynein until the end of the MT is greater than a distance $\mathcal{D}_{d_{cor}}$ from the cell cortex, at which time it begins depolymerizing.

Alternatively, if the random number, n_d, is greater than the probability of binding to dynein, P_d, the MT instead continues to grow and slips along the boundary [43, 57] (Fig. 1 v). The pushing force is described as:

$$f_i^{slip} = min\left(f_{stall}, \frac{\pi^2\kappa}{\ell_i^2}\right), \tag{3}$$

where f_{stall} is the stall force of a MT and κ is the bending rigidity of the MT. This force is also dependent on MT length, ℓ_i, such that longer MTs are more likely to buckle than shorter MTs. The pushing force felt back on the c^{th} centrosome by the $N_{c,slip}$ MTs is then:

$$\vec{F}_c^{slip} = \sum_{i=1}^{N_{c,slip}} f_i^{slip}\vec{m}_i. \tag{4}$$

MTs that push against the cell cortex also experience a slight angle change of θ and the corresponding unit direction vector $\vec{m}_i$ is then udpated. A MT will stop pushing against the cell cortex if the end of the MT is greater than a distance $\mathcal{D}_{d_{cor}}$ from the cell cortex. Alternatively, if $n_d \leq P_d$ and the end of the MT is within $\mathcal{D}_{d_{cor}}$ from the cell cortex, a pushing MT can then bind to cortical dynein.

Interpolar Forces

Interpolar MTs can experience pushing or pulling forces by being bound to opposing MTs by either Kinesin-5 (Eg5, plus-end directed) or Kinesin-14 (HSET, minus-end directed), respectively (Fig. 1 i,iii). Specifically, interpolar MTs are those that have an angle within $\pi/2$ of the vector between the centrosomes (Fig. S5 A in the Supporting Material). Forces from Eg5 are necessary for centrosome separation early in mitosis, as loss of Eg5 prevents centrosome separation and results in monopolar spindles [6, 30, 37, 58]. HSET is antagonistic to Eg5 and contributes to spindle maintenance during mitosis [36, 59].

Interpolar MTs i, j nucleated from centrosomes c, k, that are within a distance $\mathcal{D}_{Eg5}$ or $\mathcal{D}_{HSET}$ will have a probability of binding to either Eg5 or HSET and generating force. Using a Monte Carlo Method, if a random number n_{Eg5}, n_{HSET} is less than P_E, P_H, binding of Eg5 or HSET occurs, respectively. The force on each MT by either Eg5 or HSET follows Eq. (1) with stall forces $f_{0,Eg5}$, $f_{0,HSET}$ and walking velocities $v_{0,Eg5}$, $v_{0,HSET}$, respectively. The total force by MTs bound to Eg5 or HSET on centrosome c is:

$$\vec{F}_c^{Eg5} = \sum_{i=1}^{N_{c,Eg5}} -f_i^{Eg5} \frac{O_{i,j}\phi_{i,j}}{\pi \ell_i} \exp\left(-\frac{L_i}{K d_{cent}}\right) \vec{m}_i, \tag{5}$$

$$\vec{F}_c^{HSET} = \sum_{i=1}^{N_{c,HSET}} -f_i^{HSET} \frac{O_{i,j}\phi_{i,j}}{\pi \ell_i} \exp\left(-\frac{L_i}{K d_{cent}}\right) \vec{m}_i, \tag{6}$$

respectively, where $\phi_{i,j}$ is the angle of intersection between MT i on centrosome c and MT j on centrosome k, L_i is the distance between the centrosome c to the point of force application on the i^{th} MT, d_{cent} is the distance between centrosomes c and k, and $O_{i,j}$ is the overlap distance of interpolar MTs i and j (Fig. S5 B).

Spindle-Pole Dynein

In addition to its localization at the cell cortex, dynein is highly localized to spindle poles (sp) during mitosis, where it is necessary for the maintenance of MT minus-end focusing and spindle pole integrity [60, 61, 49]. We allow MTs nucleated from opposing centrosomes to have a probability $P_{d_{sp}}$ of binding to this population of dynein if they get within a distance, $\mathcal{D}_{d_{sp}}$, from the center of the centrosome. This motor-MT interaction is the same as Eq. (1). The force on centrosome c by dynein localized at spindle poles is calculated by:

$$F_c^{d_{sp}} = \sum_{i=1}^{N_{c,d_{sp}}} -f_i^{d_{sp}} \exp\left(-\frac{\ell_i}{K d_{cent}}\right) \vec{m}_i. \tag{7}$$

Centrosome Movement

Considering the above mentioned forces derived by MTs and motor protein interactions, our system of force-balance equations for the movement of centrosome c in the overdamped limit is:

$$\vec{0} = \vec{F}_c^{d_{cor}} + \vec{F}_c^{slip} + \vec{F}_c^{Eg5} + \vec{F}_c^{HSET} + \vec{F}_c^{d_{sp}} + \vec{F}_c^{r_{cent}} + \vec{F}_c^{r_{cor}} + \xi \vec{v_c}, \tag{8}$$

where $\vec{F}_c^{r_{cent}} = \frac{\vec{V}_{cent} C}{d_{cent}}$ prevents two centrosomes from occupying the same space and $\vec{F}_c^{r_{cor}} = \frac{\vec{V}_{cor} C}{d_{cor}}$ prevents a centrosome from overlapping with the boundary. $\vec{V}_{cent}$ is the vector between centrosomes (Fig. S5) while $\vec{V}_{cor}$ is the vector between the centrosome and the closest point on the cell cortex. The distance between centrosomes is d_{cent}, the minimal distance between centrosome c and the cell cortex is d_{cor}, and C is a scaling factor. We solve a system of c equations for the velocity of each centrosome, $\vec{v}_c$, and use the velocity to determine the new location of each centrosome. The velocity is scaled by a drag coefficient, ξ, to account for the viscosity of the cytoplasm within the cell. The value of ξ is calculated by $\mu/\sqrt{(\gamma)}$ where μ is the viscosity and γ is the permeability, approximated using the volume fraction of MTs in the system [62]. Our drag coefficient captures appropriate mitotic timing, as increasing drag delays centrosome separation and spindle formation (Fig. S4).

Model Analysis

Simulations and model analysis was performed in MATLAB. The base case of the model utilizes parameter values listed in Table S1 and was validated by centrosome movement when a single centrosome is present (details in Supporting Material, Fig. S2) [43, 44]. To ensure that observed centrosome movement and spindle dynamics were not an artifact of the simplified two-dimensional geometry, we compared to three-dimensional simulations (details in Supporting Material, Fig. S3 and Movie M8). To understand how model outcomes such as spindle length vary due to model stochasticity by MT dynamics and MT-motor protein binding and unbinding, we performed 10 simulations with the same initial centrosome positioning. Traces of centrosome movement over time show different trajectories (Fig. S6 A), but the velocity of centrosomes and the distance between centrosomes (spindle length) have similar trends (Fig. S6 B). Since we are primarily interested in final spindle length, we examined model results by quantifying the average final spindle length (at t=25 min) for 10, 20, 30, and 40 simulations with random initial centrosome positioning of the base case (Table 1). This analysis indicates that the average final spindle length does not change with additional simulations.

Table 1: Average (Avg) Spindle Length for Simulations (Sims) at t=25 min.

# of Sims	Avg length (μm)
10	16.37
20	16.32
30	16.33
40	16.37

Simulations achieving spindle bipolarity were those having a spindle length of at least 15 μm (the average bipolar spindle length in cells lacking stable chromosome attachments (Fig. 2 C)) at t=25 min. Monopolar spindles were characterized by spindle length being less than half the average bipolar spindle length (7.5 μm) at t=25 min.

Cell Culture, siRNA, Cell Line Generation

hTERT-immortaized Retinal Pigment Epithelial (RPE) cells were maintained in Dulbecco's Modified Essential Medium (DMEM) supplemented with 10% fetal bovine serum (FBS) and 1% Penicillin and Streptomycin and maintained at 37°C with 5% CO_2. Depletion of Nuf2 was achieved by transient transfection of a pool of four siRNA constructs (target sequences 5'-gaacgaguaaccacaauua-3', 5'-uagcugagauugugauuca-3', 5'-ggauugcaauaaaguucaa-3', 5'-aaacgauagugcugcaaga-3') at 50 nM using RNAiMAX transfection reagent according to manufacturer's instructions. Nuf2 makes up one of the four arms of the Ndc80 complex, which attaches MTs to kinetochores, along with Hec1, Spc24, and Spc25 [63]. Hec1 and Nuf2 dimerize in this complex, and knockdown of either protein destabilizes the other complex member, leading to loss of MT attachments to kinetochores [64]. Therefore, knockdown of Nuf2 was confirmed using immunofluorescence imaging with antibodies specific for Hec1 (Novus Biologicals, Littleton, CO) to assess kinetochore localization of the complex.

RPE cells stably expressing L304-EGFP-Tubulin (Addgene #64060, Watertown, MA) were generated by lentiviral transduction and placed under 10 μg/mL Puromycin selection for 5-7 days. Expression of the tagged construct was confirmed by immunofluorescent imaging [65].

Immunofluorescence Imaging

Cells were captured with a Zyla sCMOS (Oxford Instruments, Belfast, UK) camera mounted on a Nikon Ti-E microscope (Nikon, Tokyo, Japan). A 60x Plan Apo oil immersion objective was used for fixed-cell imaging and live-cell imaging of RPE cells expressing GFP-centrin to visualize centrosomes [66], and a 20x CFI Plan Fluor objective was used for live-cell imaging of RPE cells expressing GFP-tubulin [65].

Fixed-cell Imaging and Analysis

Cells seeded onto glass coverslips were rinsed briefly in phosphate buffered saline (PBS) and placed in ice cold methanol for 10 minutes at -20°C. Coverslips were washed briefly with PBS and blocked in TBS-BSA (10 mM Tris at pH 7.5, 150 mM NaCl, 1% bovine serum albumin (BSA)) for 10 minutes. Cells were incubated with primary antibodies diluted in TBS-BSA (anti-α-tubulin (1:1500; Abcam ab18251, Cambridge, UK), anti-Ndc80 (1:500; Novus Biologicals, Littleton, CO)) for 1 hour in a humid chamber. Cells were washed in TBS-BSA for 10 minutes then incubated with secondary antibodies diluted 1:1000 in TBS-BSA + 0.2 μg/mL DAPI for 45 minutes.

Fixed and live-cell image analysis was performed in NIS Elements. Fixed cell analysis of DNA area was quantified by gating a region of interest by DAPI fluorescence intensity. Spindle length was quantified by performing line scans along the long axis of the mitotic spindle and considering the spindle poles to be the two highest peaks in fluorescence intensity. Spindle morphology was characterized as bipolar, monopolar, or disorganized, where monopolar spindles were characterized by spindle length being less than half the average bipolar spindle length, and disorganized spindles had indistinguishable spindle poles. All representative images are of a single focal plane. Background was removed

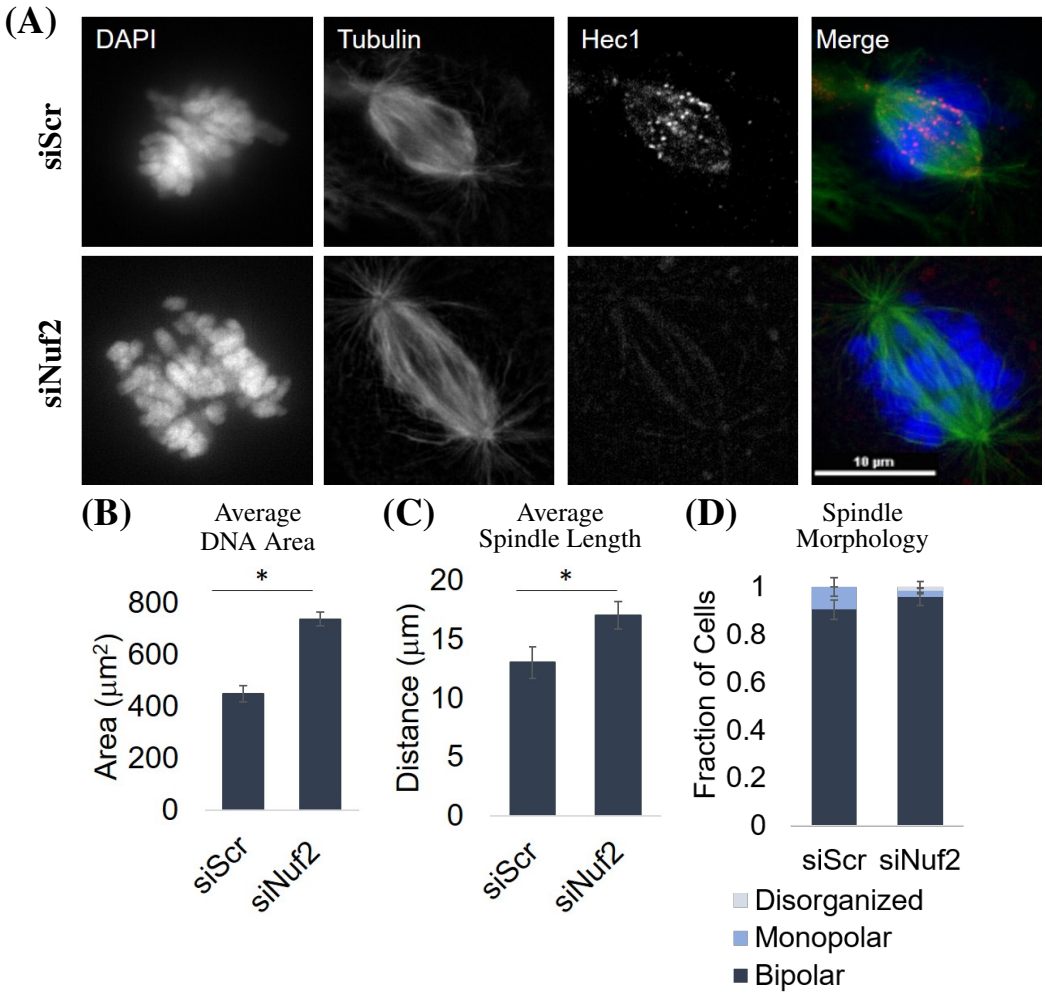

Figure 2: **Stable end-on kinetochore attachments are not required for bipolar spindle formation.** (A) Fixed-cell imaging of RPE cells stained for DAPI (DNA), Tubulin (MTs), and Hec1 (Ndc80 complex) in the control (siScr) and knockdown (siNuf2) condition. (B) Quantification of the average DAPI area in the control (siScr) and knockdown (siNuf2) condition. (C) Quantification of the average spindle length in the control (siScr) and knockdown (siNuf2) condition. (D) Quantification of the average fraction of cells with bipolar, monopolar, or disorganized spindles. All averages calculated from at least 30 cells from 3 biological replicates. Error bars are standard deviation (SD). *p¡0.05 indicates statistical significance.

and contrast was adjusted in ImageJ for fixed-cell and GFP-centrin live-cell images. Statistical analysis was performed in Excel; two-tailed Student's *t*-test was used for comparisons between two groups.

Live-cell Imaging

RPE cells stably expressing α-tubulin-EGFP were seeded onto a 6-well plate. NIS elements HCA jobs software was used to enable multi-coordinate, multi-well imaging in a single z-stack (0.67 μm per pixel) [65]. Images were captured every 5 minutes for 16 hours. Analysis was performed on at least 40 mitotic cells.

RPE cells stably expressing GFP-centrin were seeded onto glass coverslips and placed in a sealed chamber slide with 100 μl of media. Single cells entering mitosis were captured at 60x in a single z-stack (0.11 μm per pixel) every minute for the duration of mitosis.

Results and Discussion

Chromosomes are dispensable for spindle formation and maintenance

To inform our model and better define the extent to which chromosome attachments are dispensable for normal spindle structure, we performed fixed-cell image analysis of RPE cells depleted of Nuf2 (siNuf2), a protein essential for stable MT binding to kinetochores (Fig. 2 A). RPE cells are a well characterized, diploid, immortalized mammalian cell line; a useful tool for mitotic analysis. Consistent with previously described work [34, 35, 36], we find that Nuf2 depletion leads to a marked decrease in Hec1 localization at kinetochores, dispersion of chromosomes throughout the cell, and an increase in spindle length compared to the control condition, indicating failure to form stable MT attachments to kinetochores (Fig. 2 B,C). Despite these differences, spindle morphology remains largely bipolar in the Nuf2 depleted condition, with more than 90% of cells achieving bipolarity (Fig. 2 D). These data suggests that chromosomes and chromosome-derived forces are not required for bipolar spindle formation and maintenance.

A biophysical model captures bipolar spindle formation and maintenance.

To further define model requirements and validate model outputs, we performed live-cell imaging of RPE cells stably expressing an α-tubulin-EGFP transgene (Fig. 3 A). Since centrosomes are linked to spindle poles by molecular mechanisms [67, 49], we use this imaging, in addition to live-cell imaging of RPE cells expressing a GFP-tagged centrosome marker (GFP-centrin) (Fig. 3 F,G), to observe and quantify centrosome movement over time. To inform initial conditions of the model, we quantified intracentrosomal distances just prior to nuclear envelope breakdown (NEB), defined as the first point in time at which GFP-tubilin is no longer visibly excluded from the nuclear region. This analysis reveals a wide distribution, with initial centrosome distances ranging between 2.5 and 22.2 μm (Fig. 3 C). To mirror this distribution of centrosome positions in our model, we initialize centrosomes to be randomly placed at least 7.5 μm from the center of the cell, achieving a range of distances between 3.2 and 15.9 μm (Fig. 3 C).

Live-cell imaging was used to monitor centrosome movement and spindle bipolarity, and reveals that 40% of cells achieve spindle bipolarity by 5 min and 96% by 10 min (Fig. 3 D). Imaging analyses also capture centrosome separation at early time points (Fig. 3 E,F,G(i)) until an eventual bipolar spindle is achieved and maintained at an average spindle length of 12 μm (Fig. 3 E). These results are consistent with fixed-cell image analysis of RPE cells with stable MT-chromosome attachments in Fig. 2 C (siScr). By tracking individual centrosome positions in time, we calculate that they have a velocity less than 0.1 μm/sec.

Our model captures appropriate mitotic timing, with 40% of simulations achieving spindle bipolarity by 5 min and 100% by 10 min. (Fig. 3 D). An example of bipolar spindle formation is shown in Fig. 3 B and Movie M1 in the Supplementary Material. The model achieves an average bipolar spindle length of 15 μm (Fig. 3 E), consistent with with fixed-cell image analysis of cells lacking stable MT-chromosome attachments in Fig. 2 C (siNuf2). Traces of centrosome movement and centrosome velocity over time similarly resemble the biological data (Fig. 3 G,H), validating the use of our biophysical model as a tool to further understand the dynamics of mitotic spindle formation and maintenance.

Motor protein perturbations alter spindle bipolarity

The mitotic spindle has been extensively studied, and our understanding of the force requirements for spindle bipolarity has been determined primarily through experimental manipulation of force-generating motor proteins. While informative, biological assays can induce potential off-target effects that impact multiple cellular processes. To determine how motor proteins considered in our model impact spindle bipolarity, we independently perturbed motor function of Eg5, HSET, and cortical dynein by altering the binding probability of the motor β from its base case of $P_\beta = 0.5$ to $P_\beta = 0$ (Table S1, additional details in Supporting Material).

Biological data indicates that loss of Eg5 activity results in spindle pole collapse and the formation of a monopolar spindle [58]. To replicate Eg5 loss in the model, the Eg5 binding probability to MTs (P_E) was set to zero. Consistent with *in vivo* data, our simulations with loss of Eg5 activity results in rapid spindle pole collapse (Fig. 4 A(i),D, and Movie M2). In the base case of our model, dynein localized to spindle poles is dispensable for spindle bipolarity, since MT minus-ends remain anchored to centrosomes. However, our simulations of spindle dynamics in the absence of Eg5 indicate that activity of spindle-pole-localized dynein, together with HSET, remains relevant as it functions to maintain close proximity of centrosomes following spindle pole collapse (Fig. 4 B(i)).

To next test that our model accurately reflects the known role of HSET activity in mitosis, we mimic HSET depletion by setting the binding probability to MTs (P_H) equal to zero. Published biological results show that spindle length increases with HSET inhibition or depletion in the absence of stable kinetochore attachments [36]. Consistent with

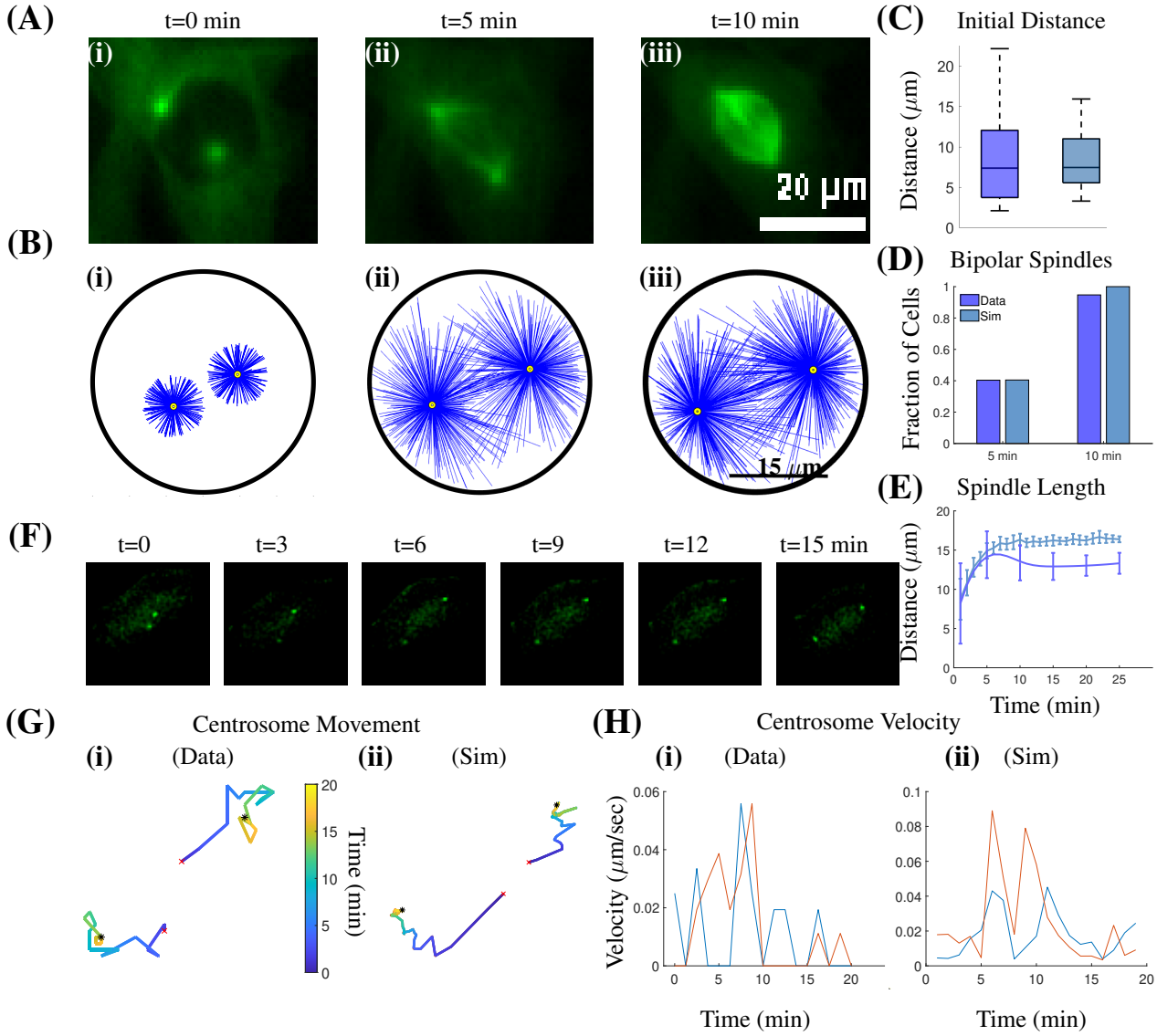

Figure 3: **Stochastic force-balance model captures centrosome movement and bipolar spindle formation.** (A) Still frames from live-cell imaging of RPE cells expressing tubulin-EGFP from the time point before nuclear envelope breakdown (NEB) at t=0 min in (i) to spindle bipolarity at t=10 min in (iii). (B) Still frames from a single simulation showing initial centrosome positioning at t=0 min in (i) to spindle bipolarity at t=10 min in (iii). The corresponding simulation is shown in Movie M1 in the Supporting Material. (C) Distributions of initial distance between spindle poles from live-cell imaging (Data) and simulations (Sim). (D) Plot of the fraction of cells (Data) and simulations (Sim) that achieve bipolarity by 5 and 10 min. (E) Plot of the spindle length over time from live-cell imaging (Data) and simulations (Sim). Error bars are standard deviation. Biological data are captured at 5 min increments; a cubic spline is used to generate the curve. All averages for (C)-(E) calculated from at least 40 cells and 40 simulations. (F) Still frames from live-cell imaging of RPE cells expressing GFP-centrin. (G) (i) Experimental traces of centrosome movement from the movie shown in (F), where color denotes time (min). (G) (ii) Traces of centrosome movement from a single simulation, where the two lines correspond to the two centrosomes, and color denotes time (min). Red 'x' is initial centrosome position, black asterisk is final centrosome position. (H) (i) Centrosome velocities over time from movie shown in (F). (H) (ii) Centrosome velocities over time from simulation shown in (G)(ii). Each line is a centrosome.

this, bipolar spindle length in our simulations increase from 15 μm for the base case to 17 μm (Fig. 4 A(ii),D and Movie M3). Analyses of force generating MTs over time reveal that increased spindle length in the absence of HSET activity is driven by Eg5 and cortical dynein (Fig. 4 B(ii)).

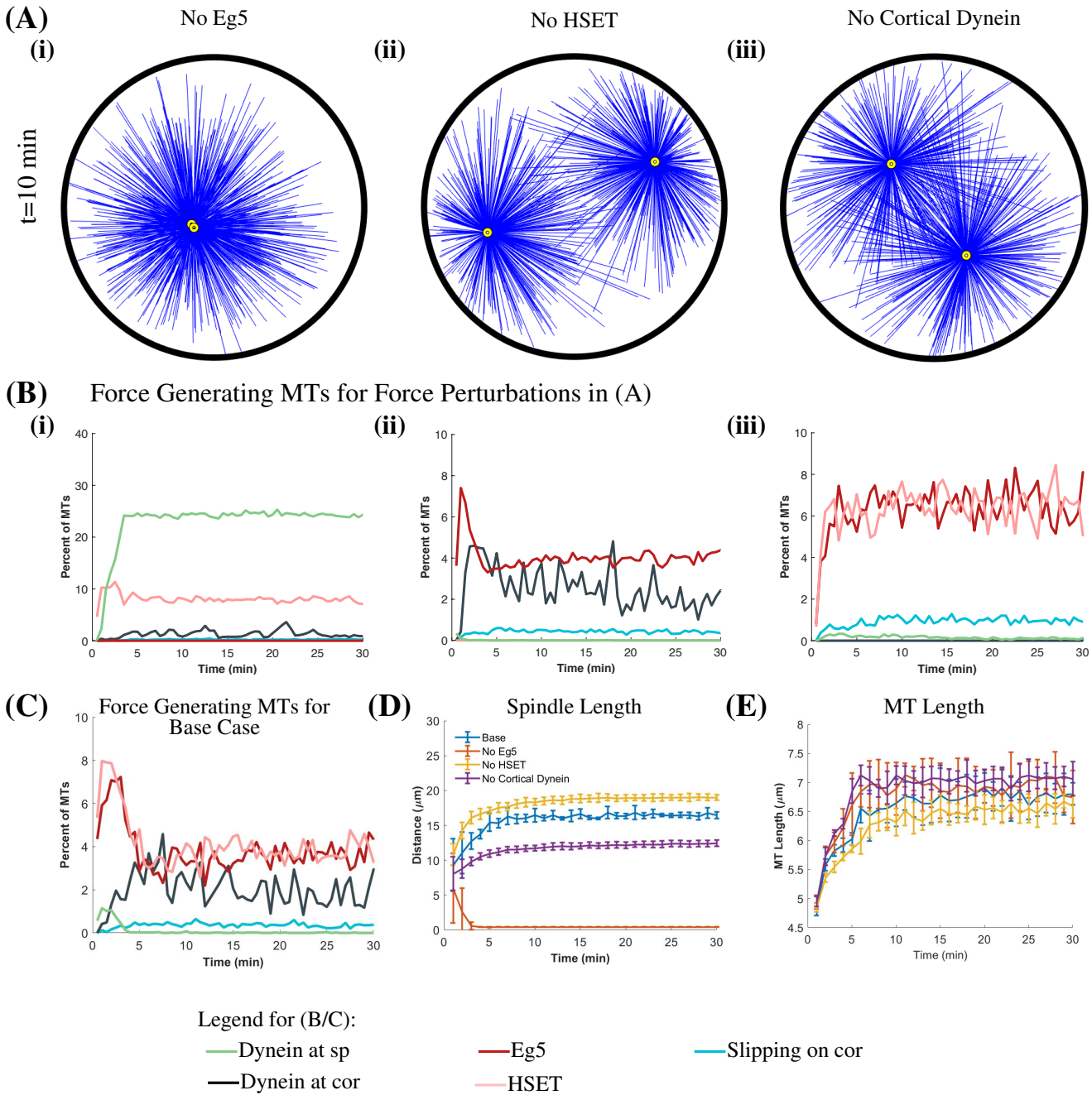

Figure 4: **Force perturbations impact spindle bipolarity.** (A) Still frame from a simulation at t=10 min with no MTs binding to: (i) Eg5, (ii) HSET, (iii) cortical dynein. The corresponding simulations are in Movies M2, M3, and M4, respectively. (B) Plot of the average percent of MTs in each force-generating state over time with no MTs binding to (i) Eg5, (ii) HSET, (iii) cortical dynein, and (C) the base case. (D) Plot of the average distance between spindle poles over time for the base case and each single force perturbation. (E) Plot of the average length of MTs over time. All averages are of 10 simulations and error bars shown correspond to standard deviation.

Due to the multiple functions of dynein at spindle poles, kinetochores, and the cell cortex [61, 49, 51, 52], biological approaches have been unable to discern the specific role of cortical dynein in bipolar spindle formation. To address this limitation in our model, cortical dynein activity was depleted by setting the binding probability to MTs (P_d) to zero. Our simulations indicate that specific loss of cortical dynein results in shorter bipolar spindles, decreased from 15 μm in the base case to 10 μm (Fig. 4 A(iii),D and Movie M4). We additionally see a 2-fold increase in MTs bound

to Eg5 and HSET when cortical dynein activity is absent compared to the base case (6% each from 3% each in the base case) (Fig. 4 B(iii),C).

Importantly, none of the single motor protein perturbations described have a significant impact on average MT length compared to the base condition (Fig. 4 E). As such, the changes in bipolar spindle length following perturbations to motor activity are strictly a result of altered forces on the centrosomes and not a consequence of limitations imposed by altered MT lengths. Combined, these results indicate that our model both captures known changes in bipolar spindle length following loss of Eg5 or HSET, and demonstrates previously undescribed changes in steady-state spindle length following loss of cortical dynein.

Cortical dynein is a primary regulator of bipolar spindle length

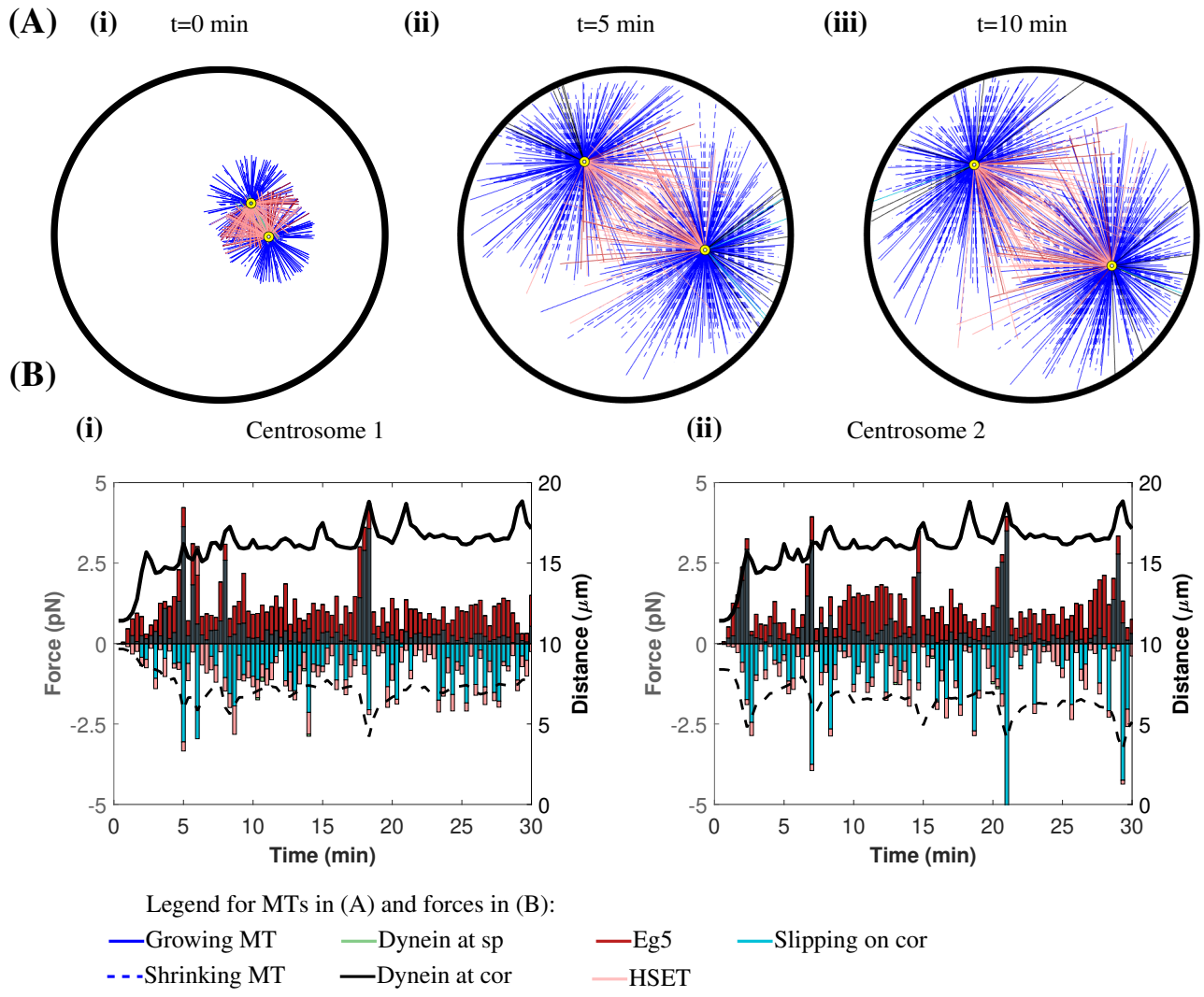

Figure 5: **Forces are dynamic over time, enabling the formation and maintenance of a bipolar spindle.** (A) Still frames from a simulation from initial centrosome positioning (i) to spindle bipolarity (iii) (full simulation in Movie M5). MT color represents its "state", defining the force that it generates. (B,C) Force plots of centrosome "1" and centrosome "2" in the direction of the vector between the two centrosomes, where a positive force brings centrosomes together and negative force pushes centrosomes apart. Black solid line shows spindle length over time and black dashed line shows the absolute minimum centrosome distance to the cell cortex over time.

The biophysical model used here to describe and explore the dynamics of bipolar spindle formation and maintenance has the benefit of discretely defined MTs, each of which can generate force depending on its length and position

relative to other intracellular components (Fig. 5 A, Movie M5). To explore how the magnitude and direction of forces change during spindle formation, we assessed each component of the force over time, with respect to $\vec{V}_{cent}$, the vector between centrosomes (Fig. S5 A) (using the projection of the total forces in the direction of $\vec{V}_{cent}$). We considered a positive force to be one that increases spindle length (i.e. Eg5/cortical dynein) and a negative force to be one that decreases spindle length (i.e. HSET/pushing on the cell cortex/dynein at spindle poles).

To visualize how forces contribute to spindle dynamics, force plots for each centrosome were overlaid with curves for spindle length and the minimal centrosome distance to the cell cortex over time (Fig. 5 B(i)-(ii)). In our base case, where we have no perturbed motor activity, we find dynamic and reproducible force-dependent changes in spindle dynamics. Our analysis shows that Eg5 activity is high at early time points (t¡5 min), indicating that early centrosome separation and bipolar spindle formation is driven by Eg5, consistent with the known biological role of Eg5 in mitosis [68, 69, 70]. Following early centrosome separation, spindle length reaches a quasi "steady-state". By observing averages over many simulations, we find that a stable spindle length is achieved (Fig. 3 E). However, analysis of single simulations shows oscillations in spindle length once a bipolar spindle has formed (Fig. 5 B). Observing the force components on each centrosome reveals that peaks in cortical dynein pulling forces coincide with both peaks in spindle length and valleys in the minimal centrosome distance to the cell cortex (Fig. 5 B). This data suggests that forces generated on centrosomes by MTs binding and being pulled by cortical dynein motor activity are responsible for changes in steady-state spindle length. We show further that MT-derived forces and bipolar spindle formation extend to three-dimensions, with dynamic changes to steady-state spindle length similarly corresponding to cortical dynein-derived forces (Fig. S3 and Movie M8).

Cortical dynein drives oscillations in spindle length after spindle bipolarity is achieved

To confirm that changes in spindle length are a consequence of cortical dynein pulling forces, we reduced cortical dynein activity in the model by altering P_d, the probability of MTs binding to dynein at the cell cortex. This analysis indicates that as the dynein binding probability is decreased, bipolar spindle length decreases (16.5 μm when $P_d = 0.5$ to 14.6 μm when $P_d = 0.3$, and 12.6 μm $P_d = 0$) and the minimal centrosome distance to the cell cortex increases (Figs. 6 A,D, S7).

To define a time-dependent relationship between bipolar spindle length and cortical dynein binding and pulling forces, we performed quantitative time-series analyses. The data is represented as a kymograph, a graphical representation of position over time, where the y-axis represents time (Fig. 6 B). In each plot, $x = 0$ is the center of the cell and $x = -15$, $x = 15$ are the cell boundaries. Red asterisks indicate centrosome position at 20 sec time intervals. We used peak prominence [71], defined as the vertical distance between the height of a peak and its lowest contour line, as a readout of significant changes in spindle length, where peaks identified as significant had a prominence of at least 1 μm. As shown in Fig. 6 B,D, oscillations in bipolar spindle length have both decreased frequency and amplitude when cortical dynein activity is decreased (when $P_d = 0.5$, 0.3, 0, the average number of prominent peaks=5, 1, 1 and peak width=35.5, 37.4, 38.7 sec, respectively). To further characterize the relationship between cortical dynein binding and bipolar spindle length, we performed cross-correlation analysis between the magnitude of cortical pulling forces on each centrosome (in the direction between centrosomes) and spindle length [72]. Results indicate that cortical dynein forces and spindle length are highly correlated at a lag of 0 min, with an average correlation coefficient of 0.62. Hence, pulling forces on the centrosome due to peaks in cortical dynein binding occurs simultaneously with significant changes in bipolar spindle length. Together, this data suggests that cortical dynein activity during mitosis is required for a *dynamic* bipolar spindle and is responsible for oscillations in steady-state spindle length.

Changes to interpolar forces, in the absence of cortical dynein, rescues bipolar spindle length but not oscillations

To further define the relationship between MT-derived forces and the maintenance of spindle bipolarity in the presence or absence of cortical dynein, we decreased HSET binding and/or increased Eg5 binding. Individually, each perturbation in the absence of cortical dynein activity partially rescues bipolar spindle length; with the most extreme conditions ($P_H = 0$ or $P_E = 1$) achieving a final spindle length of 15.2 μm and 14.2 μm, respectively, compared to the base case (positive control) at 16.5 μm and 12.6 μm when only cortical dynein activity is perturbed (negative control) (Fig. 7 A,C,E). A combination of HSET inhibition ($P_H = 0$) *and* maximum Eg5 activity ($P_E = 1$) is needed to fully restore bipolar spindle length (Fig. 7 A,B). Nevertheless, perturbations to HSET or Eg5 activity alone, or in conjunction, is insufficient to rescue oscillations in pole-to-pole distance in the absence of cortical dynein, reaffirming the requirement of cortical dynein for changes in bipolar spindle length (Fig. 7 C,E).

We performed the same perturbations to motor activity in the presence of cortical dynein to confirm that dynein activity is required for oscillations in bipolar spindle length. Here, these perturbations contribute to additive changes in spindle

length, increasing from 16.5 μm in the base case to 19.9 μm in the most extreme condition ($P_H = 0$, $P_E = 1$) (Fig. 7 B,E). Importantly, additional force perturbations to HSET or Eg5 activity do not impact oscillations in bipolar spindle length in the presence of cortical dynein, as the number of prominent peaks remains similar to that of the base case (Fig. 7 D,E). Together this data suggests that while spindle length is sensitive to both HSET and/or Eg5, cortical dynein remains the dominant regulator of spindle length oscillations.

Cortical dynein is required for spindle bipolarity when HSET activity is high

HSET overexpression is prominent in many cancer contexts where its expression corresponds with increased cell proliferation [73, 74]. This relationship with proliferation is independent of centrosome number, though in cancer contexts where centrosome number is amplified, HSET is additionally required to cluster extra spindle poles into a bipolar spindle [75, 76, 77, 78, 66, 79]. To model high HSET activity, we incrementally increased the HSET binding probability from its base level of $P_H = 0.5$. Our simulations indicate that spindle bipolarity is sensitive to HSET activity, such that the incidence of spindle pole collapse increases with high HSET activity, with only 40% of simulations forming a bipolar spindle when $P_H = 0.9$ and 0% when $P_H = 1$ (Fig. 8 A, Movie M6). To determine the force requirements for bipolar spindle formation in the presence of high HSET ($P_H = 0.9$), we explored a range of increasing cortical dynein activity and found that spindle bipolarity is rescued by cortical dynein activity in a concentration-dependent manner, with 80% of simulations forming a bipolar spindle when $P_d = 0.9$ (Fig. 8 B, Movie M7).

Work from other groups indicates that HSET-dependent motor activity is a dominant force in centrosome clustering once centrosomes reach a critical distance of 7-8 μm from each other, whereas centrosome pairs are not impacted by HSET activity when they are 11-12 μm apart [80]. Consistent with this, we find that centrosomes collapse when they are, on average, initially 6.7 μm apart, and instead form a bipolar spindle when intial centrosome distance is, on average, 10.4 μm apart. Together, these results indicate that high cortical dynein activity and/or a large initial centrosome distance promotes bipolar spindle formation in the presence of high HSET.

Conclusion

The biophysical model presented here forms and maintains a bipolar mitotic spindle through the balance of five MT-derived forces, including MT interactions with three key motor proteins: HSET, Eg5, and dynein (Figs. 1, 3, 5, Movie M5). Our model was based on and validated using our experimental data defining initial centrosome position and time-dependent changes in spindle bipolarity in mammalian cells (Figs. 2, 3). Biological inhibition or knockdown of Eg5 or HSET are shown to alter spindle length [36, 6, 30, 37, 58], and disruption of Eg5 or HSET binding to MTs in our model closely reflects this, demonstrating that our biphysical model captures known biological phenomena (Fig. 4).

The role of dynein activity in spindle formation and maintenance has been difficult to discern because of its localization and function at spindle poles, kinetochores, and the cell cortex during mitosis [61, 49, 51, 52]. By defining these motor populations independently in our model, we sought to specifically define the role of cortical dynein activity in spindle bipolarity. Previous work has shown that the position, orientation, and oscillatory movement of the bipolar spindle within the cell is regulated, in part, by cortical dynein [52, 51, 53]. Results from our model further indicate that cortical dynein activity positively influences average spindle length and promotes oscillations in pole-to-pole distance over time (Fig. 4, 6). While decreased bipolar spindle length in the absence of cortical dynein can be rescued by additional force perturbations to HSET and/or Eg5 activity, dampened spindle length oscillations are not restored, suggesting that cortical dynein is essential for this behavior (Fig. 7). Additionally, we find that high cortical dynein activity is required for bipolar spindle formation when HSET activity is also high (Fig. 8), as has been described in some cancer contexts [74, 76, 73].

Failure in cell division or defects in chromosome segregation generates cells with abnormal, and sometimes double, the number of chromosomes and centrosomes. These defects contribute to tumor heterogeneity and cancer progression [81]. Additional chromosomes pose a challenge for mitotic cells, as they require larger spindles to ensure that all chromosomes are associated with MTs prior to anaphase onset [82, 83, 84, 85]. We propose that dynamic changes in bipolar spindle length, driven by cortical dynein activity, contributes to the spindle length requirements for chromosome capture and alignment, with particular relevance to cancer contexts where chromosome number is increased. In cancer contexts where supernumerary centrosome are present, HSET-dependent centrosome clustering promotes bipolar spindle formation [75, 76, 77, 78, 66, 79]. High HSET levels have also been reported in cancer cells independent of centrosome number, although the functional implications of high HSET activity in this context remains unclear [73, 74]. Our results indicate that, when HSET activity is high, cortical dynein activity is required for bipolar spindle formation even when only two centrosomes are present. Therefore, we speculate that cancer cells having high

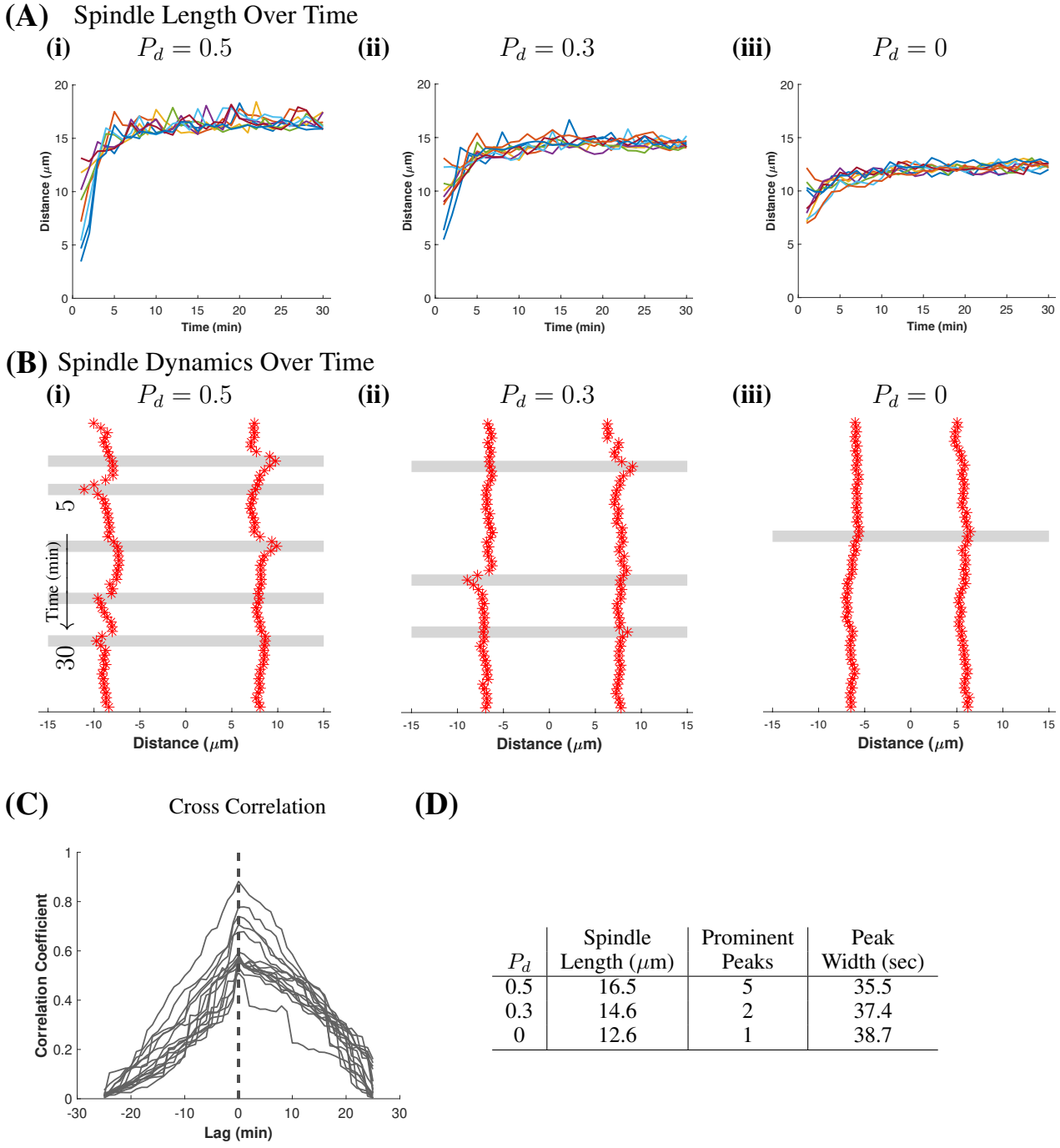

P_d	Spindle Length (μm)	Prominent Peaks	Peak Width (sec)
0.5	16.5	5	35.5
0.3	14.6	2	37.4
0	12.6	1	38.7

Figure 6: **Cortical dynein regulates spindle length and bipolar spindle dynamics.** (A) Curves of spindle length over time for 10 simulations with a dynein binding probability of 0.5 in (i), 0.3 in (ii), and 0 in (iii). (B) Representative kymograph of a single simulation with dynein binding probability 0.5 in (i), 0.3 in (ii), and 0 in (iii) from 5 to 30 minutes. Red asterisks are centrosome position plotted every 20 seconds, gray bars indicate prominent peaks in spindle length. (C) Cross correlation analysis of spindle length and magnitude of cortical dynein forces (in the direction between centrosomes). Each gray line is a centrosome, traces from 10 simulations are shown. Black vertical dashed line represents the average maximum correlation coefficient (at t=0 min). (D) Table showing average spindle length, number of prominent peaks, and width of prominent peaks from 10 simulations for each dynein binding probability.

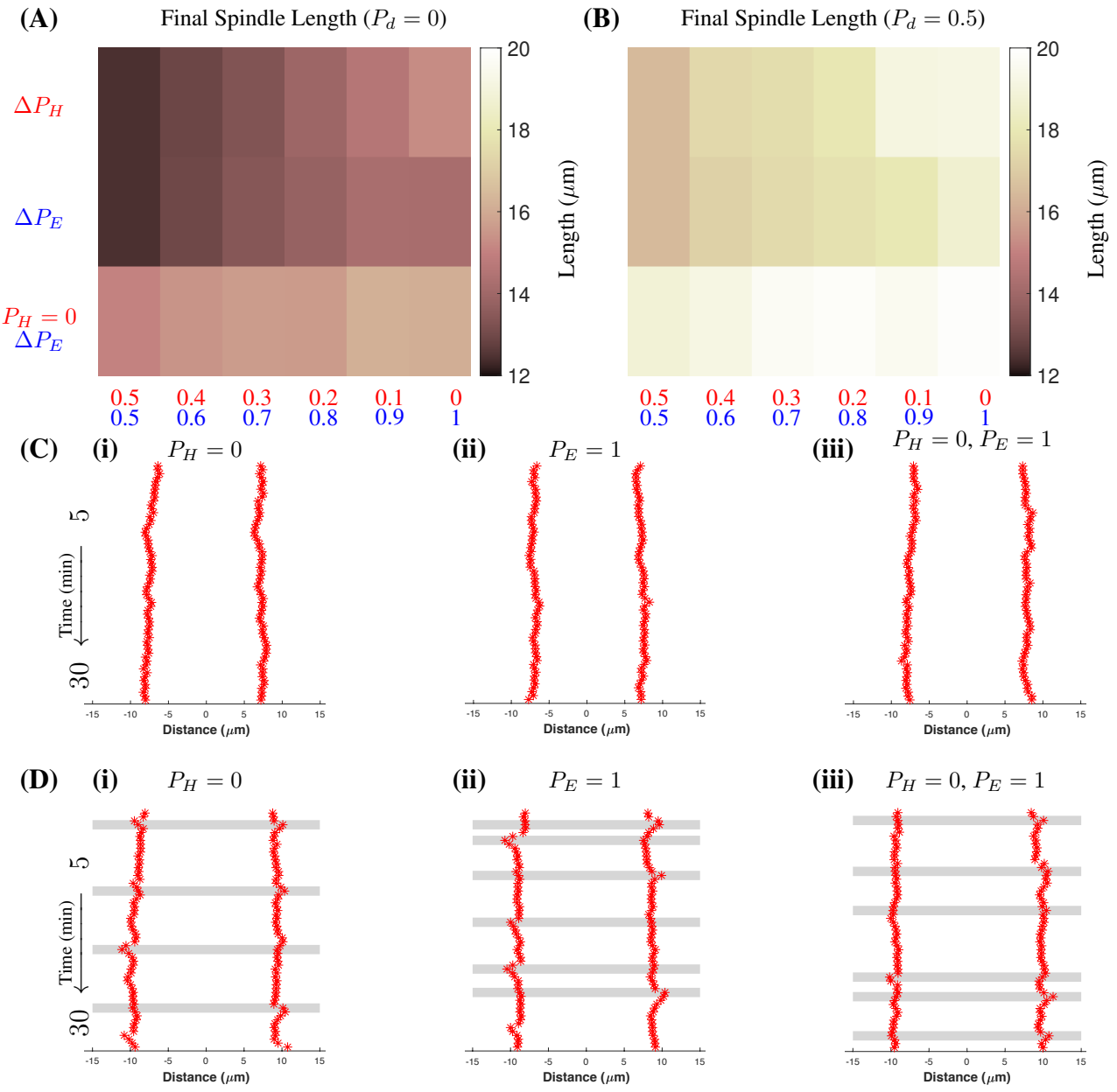

(E)

Condition	$P_d = 0.5$	$P_d = 0$	$P_d = 0$ $P_H = 0$	$P_d = 0$ $P_E = 1$	$P_d = 0$ $P_H = 0$ $P_E = 1$	$P_H = 0$	$P_E = 1$	$P_H = 0$ $P_E = 1$
Spindle Length (μm)	16.5	12.6	14.2	15.2	16.1	19.2	18.7	19.9
Prominent Peaks	5	1	1	1	1	4	4	5
Peak Width (sec)	35.5	38.7	43.6	35.5	36.4	31.3	35.2	31.7

Figure 7: **Force perturbations rescue spindle length, but not spindle dynamics, in the absence of cortical dynein.** (A,B) Heat maps showing the average final spindle length under varied conditions, in the absence (A) or presence (B) of cortical dynein. ΔP_H and ΔP_E represent the changes in HSET and/or Eg5 binding probabilities, respectively, where the probabilities are shown below the heatmap in red (ΔP_H) and blue (ΔP_H). (C) Representative kymographs of varied Eg5/HSET binding probabilities, in the absence (C) or presence (D) of cortical dynein. Gray bars indicate prominent peaks in spindle length, kymographs in (C) have no prominent peaks. (E) Table of average final spindle length, average number of prominent peaks, and average peak width under different conditions. All data averaged over 10 simulations for each condition.

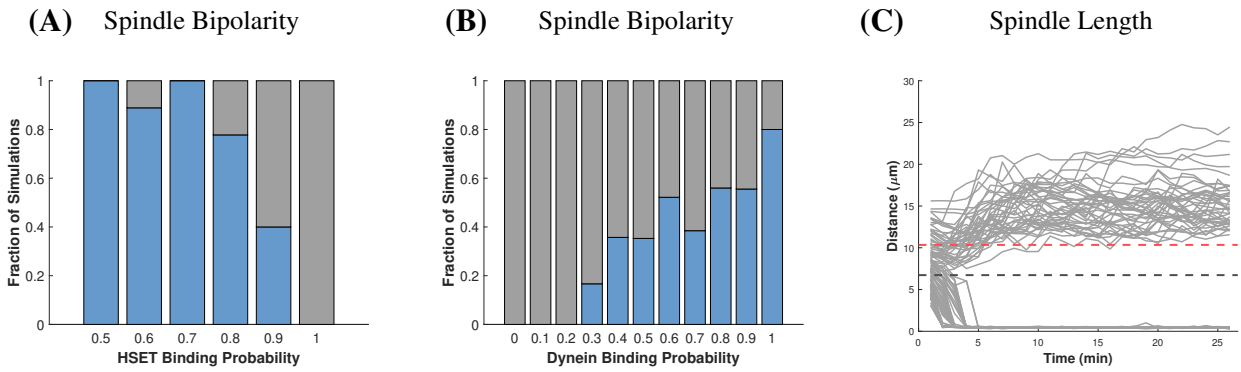

Figure 8: **High cortical dynein promotes spindle bipolarity in the presence of high HSET.** (A) Fraction of simulations that form a bipolar spindle with varying levels of HSET (example simulation of high HSET and base dynein in Movie M6). (B) Fraction of simulations that form a bipolar spindle in the presence of high HSET ($P_{HSET} = 0.9$) with varying levels of cortical dynein (example simulation of high HSET and high cortical dynein in Movie M7). (C) Plots of spindle length over time of simulations with high HSET ($P_{HSET} = 0.9$) and varying levels of cortical dynein that have simulations that form a bipolar spindle ($0.2 < P_d \leq 1$). Red dashed line is the average initial distance of centrosomes that separate (10.4 μm) and black dashed line is the average initial distance of centrosomes that collapse (6.7 μm). Data from 20 simulations for each condition.

levels of HSET, regardless of centrosome number, are dependent on cortical dynein for bipolar spindle formation and accurate cell division. Such dependencies imply that therapeutic approaches to inhibit cortical dynein may be particularly effective at limiting mitotic progression in contexts of high HSET activity, independent of centrosome and/or chromosome number.

Author Contributions

Mercadante performed experiments and carried out all model simulations. Manning designed the experiments with Mercadante and Olson developed the code for simulations with Mercadante. All authors contributed to the writing of the article and data analysis.

Acknowledgments

Results in this paper were obtained in part using a high-performance computing system acquired through NSF MRI grant DMS-1227943 to WPI. We thank Neil Ganem for supplying the RPE GFP-Centrin cell line and the members of the Manning lab for feedback throughout the writing process. ALM is supported by a Smith Family Award for Excellence in Biomedical Research and DLM is supported by a NSF-GRFP.

Supporting Material

An online supplement to this article can be found by visiting BJ Online at http://www.biophysj.org.

Supporting Citations

References (87-97) appear in the Supporting Material.

References

[1] H.Y. Wu, E. Nazockdast, M.J. Shelley, and D.J. Needleman. Forces positioning the mitotic spindle: theories, and now experiments. Bioessays, 9:1600212, 2016.

[2] E.H. Hinchliffe. The centrosome and bipolar spindle assembly. Cell Cycle, 10:3841–3848, 2011.

[3] C.L. Hueschen, S.J. Kenny, K. Xu, and S. Dumont. NuMA recruits dynein activity to microtubule minus-ends at mitosis. eLife, 6:1–26, 2017.

[4] S. Dumont and T.J. Mitchison. Force and length in the mitotic spindle. Curr. Biol., 19:R749–R761, 2009.

[5] Z.Y. She and W.X. Yang. Molecular mechanisms of kinesin-14 motors in spindle assembly and chromosome segregation. J. Cell Sci., 130:2097–2110, 2017.

[6] B.J. Mann and P. Wadsworth. Kinesin-5 regulation and function in mitosis. Trends Cell Biol., 29:66–79, 2019.

[7] R.G.H.P. van Heesbeen, M.E. Tanenbaum, and R.H. Medema. Balanced activity of three mitotic motors is required for bipolar spindle assembly and chromosome segregation. Cell Rep., 8:948–956, 2014.

[8] W.E. Channels, F.J. Nedelec, Y. Zheng, and PA. Iglesias. Spatial regulation improves antiparallel microtubule overlap during mitotic spindle assembly. Biophys. J., 94:2598–2609, 2008.

[9] E.N. Cytrynbaum, J.M. Scholey, and A.M. Mogilner. A force balance model of early spindle pole separation in drosophila embryos. Biophys. J., 84:757–769, 2003.

[10] C. Edelmaier, A.R. Lamson, Z.R. Gergley, S. Ansari, R. Blackwell, J.R. McIntosh, M.A. Glaser, and M.D. Betterton. Mechanisms of chromosome biorientation and bipolar spindle assembly analyzed by computational modeling. eLife, 9:e48787, 2020.

[11] M.E. Janson, R. Loughlin, I. Loiodice, C. Fu, D. Brunner, and F. Nedelec. Crosslinkers and motors organize dynamic microtubules to form stable bipolar arrays in fission yeast. Cell, 128:357–368, 2007.

[12] A.R. Lamson, C.J. Edelmaier, M.A. Glaser, and M.D. Betterton. Theory of cytoskeletal reorganization during cross-linker-mediated mitotic spindle assembly. Biophys. J., 116:1719–1731, 2019.

[13] J. Li and H. Jiang. Regulating positioning and orientation of mitotic spindles via cell size and shape. Phys. Rev. E, 97:012407, 2018.

[14] R. Loughlin, R. Heald, and F. Nedelec. A computational model predicts xenopus meiotic spindle organization. J. Cell Biol., 191:1239–1249, 2010.

[15] S. Sutradhar, S. Basu, and R. Paul. Intercentrosomal angular separation during mitosis plays a crucial role for maintaining spindle stability. Phys. Rev. E, 92:042714, 2015.

[16] E.J. Banigan, K.K. Chiou, E.R. Ballister, A.M. Mayo, M.A. Lampson, and A.J. Liu. Minimal model for collective kinetochore-microtubule dynamics. Proc. Natl. Acad. Sci. U.S.A., 112:12699–12704, 2015.

[17] O. Campas and P. Sens. Chromosome oscillation in mitosis. Phys. Rev. Lett., 97:128102, 2006.

[18] G. Civelekoglu-Scholey, D.J. Sharp, A. Mogilner, and J.M. Scholey. Model of chromosome motility in Drosophila embryos: adaptation of a general mechanism for rapid mitosis. Biophys. J., 90:3966–3982, 2006.

[19] A. Dinarina, C. Pugieux, M.M. Corral, M. Loose, J. Spatz, E. Karsenti, and F. Nedelec. Chromatin shapes the mitotic spindle. Cell, 138:502–513, 2009.

[20] V. Magidson, R. Paul, N. Yang, J.G. Ault, C.B. O'Connell, I. Tikhonenko, B.F. McEwen, A. Mogilner, and A. Khodjakov. Adaptive changes in the kinetochore architecture facilitate proper spindle assembly. Nat. Cell Biol., 17:1134–1144, 2015.

[21] R. Wollman, E.N. Cytrynbaum, J.T. Jones, T. Meyer, J.M. Scholey, and A. Mogilner. Efficient chromosome capture requires a bias in the 'search-and-capture' process during mitotic-spindle assembly. Curr. Biol., 15:828–832, 2005.

[22] I. Brust-Mascher, G. Civelekoglu-Scholey, M. Kwon, A. Mogilner, and J.M. Scholey. Model for anaphase B: role of three mitotic motors in a switch from poleward flux to spindle elongation. Proc. Natl. Acad. Sci. U.S.A., 101:15938–15943, 2004.

[23] C. Kozlowski, M. Srayko, and F. Nedelec. Cortical microtubule contacts position the spindle in c. elegans embryo. Cell, 129:499–510, 2007.

[24] J.J. Ward, H. Roque, C. Antony, and F. Nedelec. Mechanical design principles of a mitotic spindle. eLife, 3:e03398, 2014.

[25] N.P. Ferenz, R. Paul, C. Fagerstrom, A. Mogilner, and P. Wadsworth. Dynein antagonizes Eg5 by crosslinking and sliding antiparallel microtubules. Curr. Biol., 19:1833–1838, 2009.

[26] H. Jiang. Cell size modulates oscillation, positioning, and length of mitotic spindles. Sci. Rep., 5:1–10, 2015.

[27] J. Li and H. Jiang. Geometric asymmetry induces upper limit of mitotic spindle size. Biophys. J., 112:1503–1516, 2017.

[28] F. Nedelec. Computer simulations reveal motor properties generating stable antiparallel microtubule interactions. J. Cell Biol., 158:1005–1015, 2002.

[29] V Mountain and D.A. Compton. Dissecting the role of molecular motors in the mitotic spindle. New ANAT., 261:14–24, 2000.

[30] D.J. Sharp, G.C. Rogers, and J.M. Scholey. Microtubule motors in mitosis. Nature, 407:41–47, 2000.

[31] R. Blackwell, C. Edelmaier, O. Sweez-Schindler, A. Lamson, Z.R. Gergely, E. O'Toole, A. Crapo, L.E. Hough, J.R. McIntosh, M.A. Glaser, and M.D. Betterton. Physical determinants of bipolar mitotic spindle assembly and stability in fission yeast. Cell Biol, 3:e1601603, 2017.

[32] E. Nazockdast, A. Rahimian, D. Needleman, and M. Shelley. Cytoplasmic flows as signatures for the mechanics of mitotic positioning. Molec. Biol. Cell, 28:3261–3270, 2017.

[33] J. Zhou, J. Yao, and H.C. Joshi. Attachment and tension in the spindle assembly checkpoint. J. Cell Sci., 115:3547–3555, 2002.

[34] J.G. DeLuca, B. Moree, J.M. Hickey, J.V. Kilmartin, and E.D. Salmon. hnuf2 inhibition blocks stable kinetochore-microtubule attachment and induces mitotic cell death in HeLa cells. J. Cell Biol., 159:549–555, 2002.

[35] A.L. Manning and D.A. Compton. Mechanisms of spindle-pole organization are influenced by kinetochore activity in mammalian cells. Curr. Biol., 17:260–265, 2007.

[36] S. Cai, L.N. Weaver, S.C. Ems-McClung, and C.E. Walczak. Kinesin-14 family proteins hset/xtck2 control spindle length by cross-linking and sliding microtubules. Mol Biol Cell, 20:1348–1359, 2009.

[37] T.M. Kapoor, T.U. Mayer, M.L. Coughlin, and T.J. Mitchison. Probing spindle assembly mechanisms with monastrol, a small molecule inhibitor of the mitotic kinesin, Eg5. J. Cell Biol., 150:975–988, 2000.

[38] W.T. Silkworth, I.K. Nardi, R. Paul, A. Mogilner, and D. Cimini. Timing of centrosome separation is important for accurate chromosome segregation. Mol. Biol. Cell, 23:401–411, 2011.

[39] Y. Zhang, O. Foreman, D.A. Wigle, F. Kosari, G. Vasmatzis, J.L. Salisbury, J. Van Deusen, and P.J. Galardy. Usp44 regulates centrosome positioning to prevent aneuploidy and suppress tumorigenesis. J. Clin. Invest., 122:4362–4374, 2012.

[40] M. Biro, Y. Romeo, S. Kroschwald, M. Bovellan, A. Boden, J. Tcherkezian, P.P. Roux, G. Charras, and E.K. Paluch. Cell cortex composition and homeostasis resolved by integrating proteomics and quantitative imaging. Cytoskeleton, 70:741–754, 2013.

[41] O.M. Lancaster, M. Le Berre, A. Dimitracopoulos, D. Bonazzi, E. Zlotek-Zlotkiewicz, R. Picone, T. Duke, M. Piel, and B. Baum. Mitotic rounding alters cell geometry to ensure efficient bipolar spindle formation. Dev. Cell, 25:270–283, 2013.

[42] P. Kunda, A.E. Pelling, T. Liu, and B. Baum. Moesin controls cortical rigidity, cell rounding, and spindle morphogensis during mitosis. Curr. Biol., 18:91–101, 2008.

[43] L. Laan, N. Pavin, J. Husson, G. Romeg-Lemonne, M. van Duijn, M.P. Lopez, R.D. Vale, F. Julicher, S.L. Reck-Peterson, and M. Dogterom. Cortical dynein controls microtubule dynamics to generate pulling forces that reliably position microtubule asters. Cell, 148:502–514, 2012.

[44] L. Laan, S. Roth, and M. Dogterom. End-on microtubule-dynein interactions and pulling-based positioning of microtubule organizing centers. Cell Cycle, 11:3750–3757, 2012.

[45] M.W. Kirschner and T. Mitchison. Microtubule dynamics. Nature, 324:621, 1986.

[46] M.M. Mogensen, A. Malik, M. Piel, V. Bouckson-Castaing, and M. Bornens. Microtubule minus-end anchorage at centrosomal and non-centrosomal sites: the role of ninein. J. Cell Sci., 113:3013–3023, 2000.

[47] M.K. Gardner, M. Zanic, C. Gell, V. Bormuth, and J. Howard. Depolymerizing kinesins Kip3 and MCAK shape cellular microtubule architecture by differential control of catastrophe. Cell, 147:1092–1103, 2011.

[48] M.K. Gardner, M. Zanic, and J. Howard. Microtubule catastrophe and rescue. Curr. Opinion Cell Biol., 25:14–22, 2013.

[49] G. Goshima, F. Nedelec, and R.D. Vale. Mechanisms for focusing mitotic spindle poles by minus end-directed motor proteins. J. Cell Biol., 171:220, 2005.

[50] C.E. Walczak, I. Vernos, T.J. Mitchison, E. Karsenti, and R. Heald. A model for the proposed roles of different microtubule-based motor proteins in establishing spindle bipolarity. Curr. Biol., 8:903–913, 1998.

[51] T. Kiyomitsu and I.M. Cheeseman. Chromosome-and spindle-pole derived signals generate an intrinsic code for spindle position and orientation. Nat. Cell Biol., 14:311–317, 2012.

[52] S. Kotak, C. Busso, and P.J. Gonczy. Cortical dynein is critical for proper spindle positioning in human cells. Cell Biol., 199:97–110, 2012.

[53] M. Okumura, T. Natsume, M.T. Kanemaki, and T. Kiyomitsu. Dynein-dynactin-NuMA clusters generate cortical spindle-pulling forces as a multi-arm ensemble. eLife, 7:e36559, 2018.

[54] J. Wu, G. Misra, R.J. Russell, A.J. Ladd, T.P. Lele, and R.B. Dickinson. Effects of dynein on microtubule mechanics and centrosome positioning. Mol. Biol. Cell, 22:4834–4841, 2011.

[55] K. Svoboda and S.M. Block. Force and velocity measured for single kinesin molecules. Cell, 77:773–784, 1994.

[56] S. Chatterjee, A. Sarker, A. Khodjakov, A. Mogilner, and R. Paul. Mechanics of multi-centrosomal clustering in bipolar mitotic spindles. In Press, preprint at bioRxiv 0.1101/2019.12.17.879817, 2020.

[57] A. Burakov, E. Nadezhdina, B. Slepchenko, and V. Rodinov. Centrosome positioning in interphase cells. J. Cell Biol., 162:963–969, 2003.

[58] T.U. Mayer, T.M. Kapoor, S.J. Haggarty, R.W. King, S.L. Schreiber, and T.J. Mitchison. Small molecule inhibitor of mitotic spindle bipolarity identified in a phenotype-based screen. Science, 286:971–974, 1999.

[59] V. Mountain, C. Simerly, L. Howard, A. Ando, G. Schatten, and D. A. Compton. The kinesin-related protein, Hset, opposes the activity of Eg5 and cross-links microtubules in the mammalian mitotic spindle. J. Cell Biol., 147:351, 1999.

[60] R. Tan, P.J. Foster, D.J. Needleman, and R.J. McKenny. Cooperative accumulation of dynein-dynactin at microtubule minus-ends drives microtubule network organization. Dev. Cell, 44:233–247, 2018.

[61] J. Gaetz and T.M. Kapoor. Dynein/dynactin regulate metaphase spindle length by targeting depolymerizing activities to spindle poles. J. Cell Biol., 166:465–471, 2004.

[62] K. Luby-Phelps, S. Mujumdar, R.B. Mujumdar, L.A Ernst, W. Galbraith, and A.S. Waggoner. A novel fluorescence ratiometric method confirms the low solvent viscosity of the cytoplasm. Biophys. J., 65:236–242, 1993.

[63] R.R. Wei, P.K. Sorger, and S.C. Harrison. Molecular organization of the ndc80 complex, and essential kinetochore component. Proc Natl Acad Sci USA, 102:5363–5367, 2005.

[64] T. Hori, T. Haraguchi, Y. Hiraoka, H. kimura, and T. Fukagawa. Dynamic behavior of nuf2-hec1 complex that localizes to the centrosome and centromere and is essential for mitotic progression in mitotic cells. J Cell Sci., 116:3347–3362, 2003.

[65] D.L. Mercadante and A.L. Crowley, E.A. amd Manning. Live cell imaging to assess the dynamics of metaphase timing and cell fate following mitotic spindle perturbations. J. Vis. Exp, 151, 2019.

[66] N.J. Ganem, S.A. Godinho, and D. Pellman. A mechanism linking extra centrosomes to chromosomal instability. Nature, 460:278–282, 2009.

[67] S.A. Endow, R. Chandra, D.J. Komma, A.H. Yamamoto, and E.D. Salmon. Mutants of the drosophila ncd microtubule motor protein cause centrosomal and spindle pole defects in mitosis. J. Cell Sci., 107:859–867, 1994.

[68] A.S. Kashina, R.J. Baskin, D.G. Cole, K.P. Wedaman, W.M. Saxton, and J.M. Scholey. A bipolar kinesin. Nature, 379:270–272, 2009.

[69] L.C. Kapitein, E.J. Peterman, B.H. Kwok, J.H. Kim, T.M. Kapoor, and C.F. Schmidt. A bipolar mitotic kinesin moves on both microtubules that it crosslinks. Nature, 435:114–118, 2005.

[70] M.E. Tanenbaum and R.H. Medema. Mechanisms of centrosome separation and bipolar spindle assembly. Dev. Cell, 19:797–806, 2010.

[71] MathWorks. findpeaks, 2007.

[72] MathWorks. xcorr, 2009.

[73] V. Pannu, P. Rida, A. Ogden, R. Turaga, S. Donthamsetty, N. Bowen, K. Rudd, M. Gupta, M. Reid, G. Cantauria, C. Walczak, and R. Aneja. Hset overexpression fuels tumor progression via centrosome clustering-independent mechanisms in breast cancer patients. Oncotarget, 6:6079–6091, 2015.

[74] J. Klaylein-Sohn, B. Pollinger, M. Ohmer, F. Hofmann, E. Nigg, B. Hemmings, and M. Wartmann. Acentrosomal spindle organization renders cancer cells dependent on the kinesin hset. J. Cell Sci., 125:5391–5402, 2012.

[75] J.Y. Chan. A clinical overview of centrosome amplification in human cancers. Int. J. Biol. Sci., 7:1122–1144, 2011.

[76] J. Kwon, S. Godinho, N.S. Chandhok, N.J. Ganem, A. Azioune, M. Thery, and D. Pellman. Mechanisms to suppress multipolar divisions in cancer cells with extra centrosomes. Genes Dev., 22:2189–2203, 2008.

[77] B. Navarro-Serer, E.P. Childers, N.M. Hermance, D. Mercadante, and A.L. Manning. Aurora A inhibition limits centrosome clustering and promotes mitotic catastrophe in cells with supernumerary centrosomes. Oncotarget, 10:1649–1659, 2019.

[78] N.J. Quintyne, J.E. Reing, D.R. Hoffelder, S.M. Gollin, and W.S. Saunders. Spindle multipolarity is prevented by centrosomal clustering. Science, 307:127–129, 2005.

[79] F. Galimberti, S.L. Thompson, S. Ravi, D.A. Compton, and E. Dmitrovsky. Anaphase catastrophe is a target for cancer therapy. Clin. Cancer Res., 17:1218–1211, 2011.

[80] A.D. Rhys, P. Monteiro, C. Smith, M. Vaghela, T. Arnandis, T. Kato, B. Leitinger, E. Sahai, A. McAinsh, G. Charras, and S.A. Godinho. Loss of E-cadherin provides tolerance to centrosome amplification in epithelial cancer cells. J. Cell Biol., 217(1):195–209, 2018.

[81] L. Sansregret and C. Swanton. The role of aneuploidy in cancer evolution. CSH PERSPECT MED, 7:a028373, 2017.

[82] NJ Ganem, Z Storchova, and D Pellman. Tetraploidy, aneuploidy and cancer. Curr. Opin. Genet. Dev., pages 157–162, 2007.

[83] AY Kuznetsova, GK Seget, K ad Moeller, MS de Pagter, JA de Roos, R Durrbaum, C Kuffer, S Muller, GJ Zaman, WP Kloosterman, and Z Storchova. Chromosomal instability, tolerance of mitotic errors and multidrug resistance are promoted by tetraploidization in human cells. Cell Cycle, 14:2810–2820, 2015.

[84] Z Storchova and C Kuffer. The consequences of tetraploidy and aneuploidy. J. Cell Sci., 121:3659–3866, 2208.

[85] CF Yang, WY Tsai, WA Chen, KW Liang, CJ Pan, PL Lai, PC Yang, and HC Huang. Kinesin-5 contributes to spindle-length scaling in the evolution of cancer toward metastasis. Sci Rep, 6:35767, 2016.

[86] M. Piehl and L. Cassimeris. Organization and dynamics of growing microtubule plus ends during early mitosis. Mol. Biol. Cell, 14:916–925, 2003.

[87] T.J. Mitchison. Polewards microtubule flux in the mitotic spindle: evidence from photoactivation of fluorescence. J. Cell Biol., 109:637–642, 1989.

[88] Y.A. Komarova, A.S. Akhmanova, S. Kojima, N. Galjart, and G.G. Borisy. Cytoplasmic linker proteins promote microtubule rescue in vivo. J. Cell Biol., 159:589–599, 2002.

[89] R. Ma, L. Laan, M. Dogterom, N. Pavin, and F. Julicher. General theory for the mechanics of confined microtubule asters. New J. Phys., 16:013018, 2013.

[90] M. Piehl, U.S. Tulu, P. Wadsworth, and L. Cassimeris. Centrosome maturation: measurement of microtubule nucleation throughout the cell cycle by using GFP-tagged EB1. Proc. Natl. Acad. Sci. U.S.A., 101:1584–1588, 2004.

[91] M.M. Elshenawy, J.T. Canty, L. Oster, L.S. Ferro, Z. Zhou, S.C. Blanchard, and A. Yildiz. Cargo adaptors regulate stepping and force generation of mammalian dynein-dynactin. Nat Chem Biol, 15:1093–1101, 2019.

[92] L. Urnavicius, C.K. Lau, M.M. Elshenawy, E. Morales-Rios, C. Motz, A. Yildiz, and A.P. Carter. Cryo-em shows how dynactin recruits two dyneins for faster movement. Nature, 554:202–206, 2018.

[93] Y. Shimamoto, S. Forth, and T.M. Kapoor. Measuring pushing and braking forces generated by ensembles of kinesin-5 crosslinking two microtubules. Dev. Cell, 34:669–681, 2015.

[94] J. Li, L. Cheng, and H. Jiang. Cell shape and intercellular adhesion regulate mitotic spindle orientation. Mol Biol Cell, 30, 2019.

[95] J. Roostalu, J. Rickman, C. Thomas, F. Nedelec, and T. Surrey. Determinants of polar versus nematic organization in networks of dynamic microtubules and mitotic motors. Cell, 175:796–808, 2018.

[96] G.Y. Chen, Y.J. Kang, S.A. Gayek, W. Youyen, E. Tuzel, R. Ohi, and W.O. Hancock. Eg5 inhibitors have contrasting effect on microtubule stability and metaphase spindle integrity. ACS Chem. Biol., 12:1038–1046, 2017.

[97] F. Decker, D. Oriola, B. Dalton, and J. Bruges. Autocatalytic microtubule nucleation determines the size and mass of xenopus laevis egg extract spindle. eLife, 7:e31149, 2018.

Supporting Material

Modeling reveals cortical dynein-dependent oscillations in bipolar spindle length

D Mercadante, AL Manning, SD Olson

Additional Model Details

Model Initialization and Algorithm

At the start of the simulation, random initial locations were chosen for centrosomes that matched the distribution from experimental data (Fig. 3 C). 300 MTs, randomly distributed between the two centrosomes, were initialized with angles α and lengths ℓ chosen from a uniform distribution, $\alpha \in \mathcal{U}[0, 2\pi)$ and $\ell \in [0, 0.5]$. At each time step, new MTs are nucleated (up to the tubulin limit). The states of each MT are updated based on the stochastic rules (e.g. Monte Carlo binding to cortical dynein if close to cortex based on binding probability P_d). The states and configuration of the MTs then lead to the current forces on each centrosome. The force-balance equations are solved to determine the new locations of each centrosome. The MTs are then updated based on state (growing, shrinking, angle of vector direction changes). This is repeated at each time step until $t = 30$ min is reached.

Microtubules

MTs undergo rescue (switch from shrinking to growing) at a rate k_1 and undergo catastrophe (switch from growing to shrinking) at a MT-length dependent rate k_2, defined as $k_{2_i} = sv_g\ell_i$, where s is a scaling factor, ℓ_i is the length of the i^{th} MT, and dt is the time step [48]. Following a standard Monte Carlo method, we choose $n_2 \in \mathcal{U}[0, 1]$ and the i^{th} growing MT undergoes catastrophe if $n_2 \leq k_2^*$, where $k_2^* = 1 - e^{-k_{2_i}dt}$ [13]. Similarly, shrinking MT i will be rescued if $n_1 \leq k_1^*$ where $k_1^* = 1 - e^{-k_1 dt}$. MTs that fail to undergo rescue depolymerize completely and are no longer considered in the system when $\ell_i \leq v_g dt$. We note that there are a few exceptions. Binding of Eg5 and HSET stabilizes MT plus-ends [96]; to model this behavior in our simulations, MTs that are bound to Eg5 or HSET continue to grow from their plus-ends but cease to undergo catastrophe.

Nucleation of MTs occurs at a rate MT_{nuc} and is then prevented once MTs exceed a total length of M, accounting for limited tubulin in the system [97]. Fig. S1 compares the limited tubulin base case to the case of unlimited tubulin. Limiting tubulin increases computational efficiency and as can be seen from the average spindle length in S1(A) and average MT length in S1(B), similar trends are observed. The major difference is the average number of MTs over time, as shown in S1(C); MT forces increase but on average, they result in the same spindle length, which is the major focus of this study.

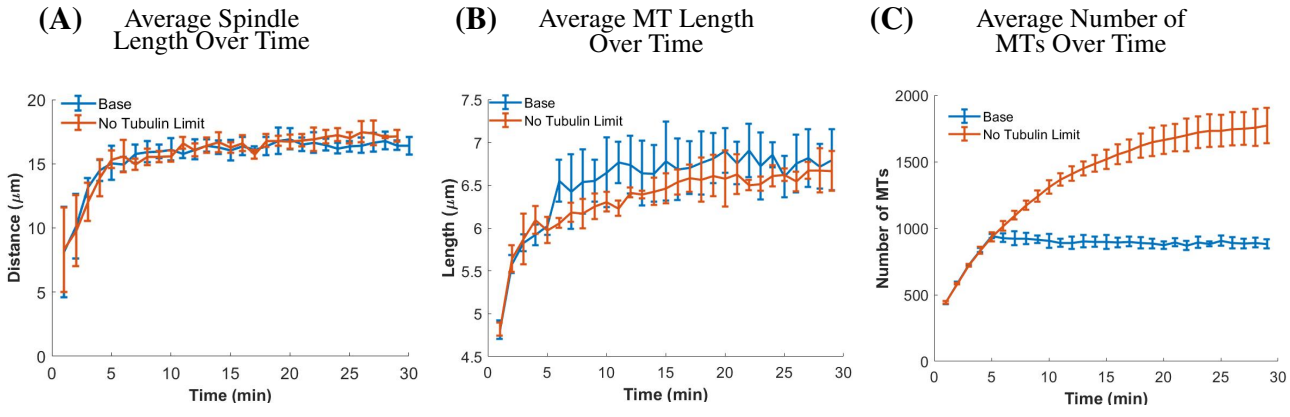

Figure S1: **Limiting tubulin impacts MT number but not spindle length or MT length.** Traces over time for the base case and case without limiting tubulin for spindle length (A), MT length (B), and MT number (C). Averages calculated for 10 simulations. Error bars are standard deviation.

Table S1: Parameter Values

Parameter	Value	Description	Reference
Microtubules			
v_g	0.183 μms^{-1}	MT growth velocity (+ ends)	[86, 54]
v_s	0.3 μms^{-1}	MT shrinking velocity (+ ends)	[54]
v_b	0.057 μms^{-1}	MT shrinking velocity (+ ends) bound to cortical dynein	[43]
v_f	0.0083 μms^{-1}	Poleward flux (− ends)	[87]
k_1	0.167 s^{-1}	Rescue frequency	[54, 88]
κ	3.3 pNμm^2	Bending rigidity	[43]
f_{stall}	5 pN	Stall force of MTs	[89]
MT_{nuc}	2 s^{-1}	MT nucleation rate per centrosome	[90]
θ	10π/180	Slipping MT angle change	
M	6000 μm	Maximum sum of MT lengths	
Motor Proteins			
Dynein			
$f_{0,d}$	3.6 pN	Stall force of dynein	[91]
$v_{0,d}$	0.86 μms^{-1}	Walking velocity of dynein	[92, 91]
P_d	0.5	Probability of binding to cortical dynein	
$P_{d_{sp}}$	0.5	Probability of binding to spindle pole dynein	
$\mathcal{D}_d$	$4v_g(dt)$ μm	Distance required for binding to dynein	
$\mathcal{D}_{d_{sp}}$	1 μm	Distance required for binding to dynein at spindle poles	
Kinesin-5 (Eg5)			
$f_{0,Eg5}$	1.5 pN	Stall force of Eg5	[93]
$v_{0,Eg5}$	0.2 μms^{-1}	Walking velocity of Eg5	[94]
P_E	0.5	Probability of binding to Eg5	
Kinesin-14 (HSET)			
$f_{0,HSET}$	1.1 pN	Stall force of HSET	[95]
$v_{0,HSET}$	0.2 μms^{-1}	Walking velocity of HSET	[94]
P_H	0.5	Probability of binding to HSET	
$\mathcal{D}_{Eg5,HSET}$	$v_g dt$ μm	Distance required for binding to Eg5 or HSET	
Other			
c_r	0.3 μm	Radius of a centrosome	
$\mathcal{D}_r$	$2c_r$ μm	Distance for repulsive forces	
K	0.25	Scaling factor	
C	2 μm	Scaling for repulsive forces	
s	0.15 μm^{-1}	Scaling for catastrophe frequency	
μ	0.7 pNsμm^{-2}	Viscosity of the cytoplasm	[62]
γ	0.0012 μm^{-1}	Permeability of the cytoplasm	
ξ	20.6 pNs	Drag coefficient	

Additional Model Validation

Single Centrosome

It has been well documented that cortical pushing and pulling forces position the centrosome in the center of the cell during interphase; the time between successive mitotic divisions when only one centrosome is present. The dynamics of centrosome centering has been shown in both cells [57] and microfabricated chambers [43, 44]. To confirm that our model captures appropriate centrosome dynamics, we observed centrosome movement over time with varying concentrations of cortical dynein, as has been experimentally tested *in vitro* [43]. All parameters are the same as those listed in Table S1.

We show that a centrosome efficiently centers with our "intermediate" dynein concentration ($P_d = 0.5$); centering 82% of the time (Fig. S2 B). Centering is defined by the centrosome achieving a distance of at least 4 μm from the center of the cell. Altering cortical dynein concentration also impacts centering efficiency. Increasing dynein concentrations ($P_d = 0.75$) prevents centrosome centering, as we have increased pulling towards the boundary of the cell (Fig. S2 C). Additionally, high dynein concentrations increase average centrosome velocity (Fig. S2 D).

Alternatively, preventing MT binding to cortical dynein ($P_d = 0$) improved centering efficiency, with centrosomes centering 100% of the time (Fig. S2 A). Additionally, both the maximum centrosome velocity and the average centrosome velocity is increased compared to the intermediate dynein case (Fig. S2 D). These results are consistent with [43], who show that, with moderate MT lengths, MT centering is most efficient with no dynein and least efficient with high dynein. Together these results indicate that our model is capturing appropriate centrosome movement driven by MT-cortex derived forces.

Two Centrosomes in Three-Dimensions

Due to the computational complexity of simulating the stochastic dynamics of 1000 MTs interacting with motors and the cell cortex over the time course of 30 minutes, we focused on two-dimensional (2-d) simulations. However, we wanted to ensure that the results obtained in the 2-d representation were consistent with the 3-d simulations. The force-balance equation in Eq. (8) and MT-motor forces in Eqs. (1)-(7) all extend to 3-d. The only parameters that change from the 2-d base case (Table S1) are $\mathcal{D}_d = 2\mathcal{D}_d$ and $\mathcal{D}_{Eg5,HSET} = 2\mathcal{D}_{Eg5,HSET}$. Since we simplify MTs to a direction vector and a length, we account for deformations of the MTs by specifying a larger region for MT-motor interactions to occur for the interpolar MTs (refer to Fig. S5).

Fig. S3 highlights results for the 3-d model. Similar to the initialization of centrosome positions in the 2-d case (Fig. 3 C), we randomly initialize the two centrosomes to be 7.5 μm from the cell center with a range of centrosome distances between 2 and 15 μm (Fig. S3 A). The average spindle length from $t = 10 - 30$ minutes is 17.3 μm in 3-d (Fig. S3 A), in comparison to 16.3 μm in 2-d (Fig. 3 E). Similar oscillations are observed in spindle length (comparing 2-d base case in Fig. S4 A and Fig. S3 A). A sample trace of centrosomes with respect to time is shown in Fig. S4 B, having a mean centrosome velocity of 0.04 μm/sec; a similar time course in movement is observed in the 2-d case in Fig. 3 G(ii) with a mean centrosome velocity of 0.025 μm/sec. We show further that dynamic changes to steady-state spindle correspond to cortical dynein-derived forces (Fig. S3 C and Movie M8 for 3-d compared to Fig. 5 B for 2-d). The frequency of the spindle pole oscillations is increased for 3-d, but these oscillations are a robust phenomena.

Supporting Figures and Movies

Movie M1 Simulation of centrosome movement and bipolar spindle formation corresponding to Fig. 3 B.

Movie M2 Simulation with no Eg5 ($P_E = 0$), corresponding to Fig. 4 A(i).

Movie M3 Simulation with no HSET ($P_H = 0$), corresponding to Fig. 4 A(ii).

Movie M4 Simulation with no MTs binding to cortical dynein ($P_d = 0$), corresponding to Fig. 4 A(iii).

Movie M5 Simulation with MT-motor forces colored, corresponding to Fig. 5 A. Colored dots on the cortex correspond to locations of MTs slipping (cyan) or MTs binding to cortical dynein (black).

Movie M6 Simulation with high HSET and base dynein (Fig. 8 A).

Movie M7 Simulation with high HSET and high dynein (Fig. 8 B).

Movie M8 Three-dimensional simulation of model (Fig. S3 B).

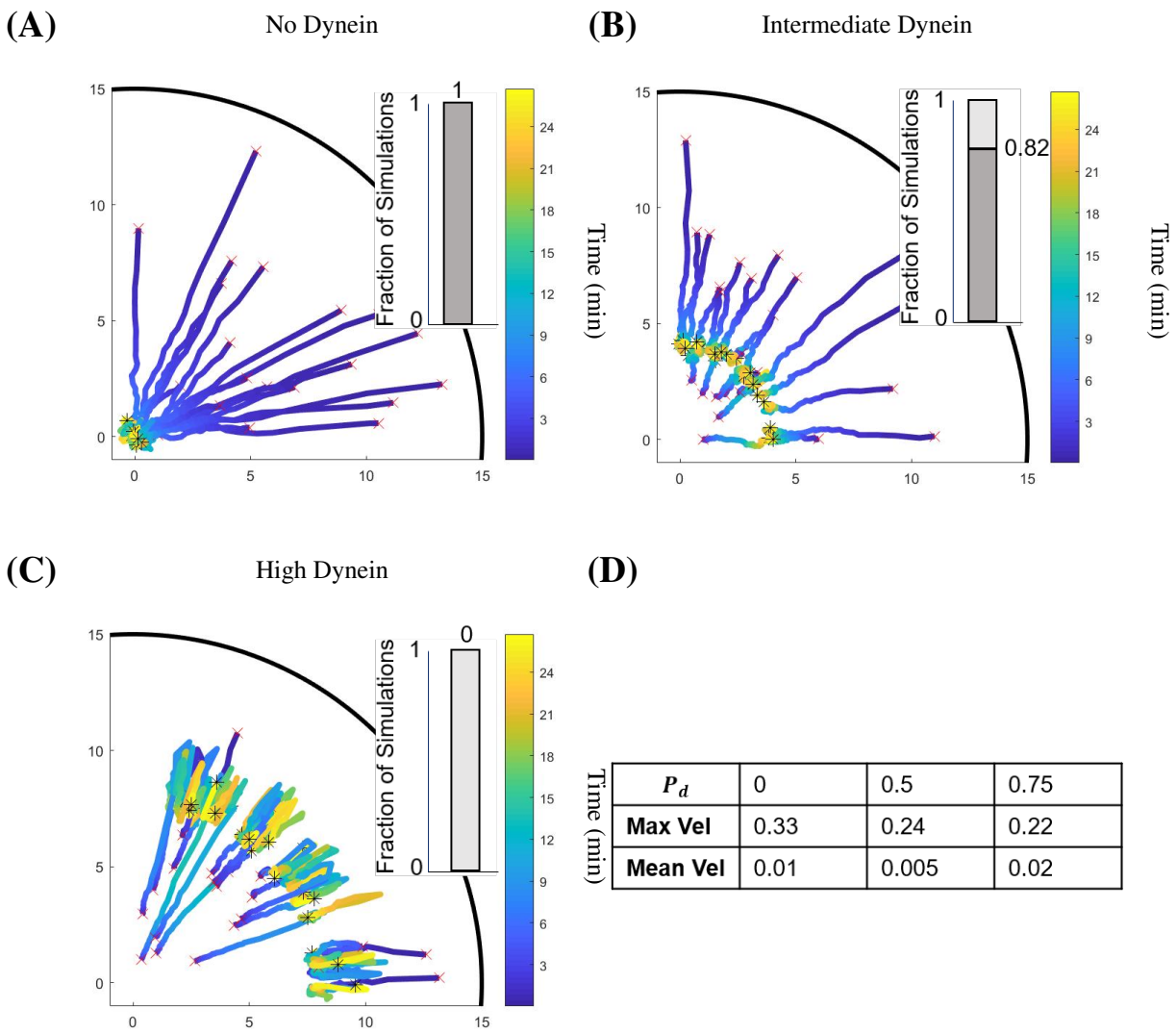

P_d	0	0.5	0.75
Max Vel	0.33	0.24	0.22
Mean Vel	0.01	0.005	0.02

Figure S2: **MT interactions with the cell cortex regulate centrosome movement and positioning.** (A) Centrosome movement traces over time with no MT binding to cortical dynein; $P_d = 0$ (B) Centrosome movement traces over time with MTs both binding to cortical dynein and pushing against the cell cortex; $P_d = 0.5$. (C) Centrosome movement traces over time with MTs binding to both cortical dynein and pushing against the cell cortex; $P_d = 0.75$. Bar plots represents the fraction of simulatons with the centrosome centered at the final time point. Dark gray bar represents centered centrosomes, light gray bar represented un-centered centrosomes. Red 'x' is initial centrosome position, black asterisk is final centrosome position. (D) Table showing the average maximum and mean centrosome velocities in the different conditions. All averages calculated from 50 simulations

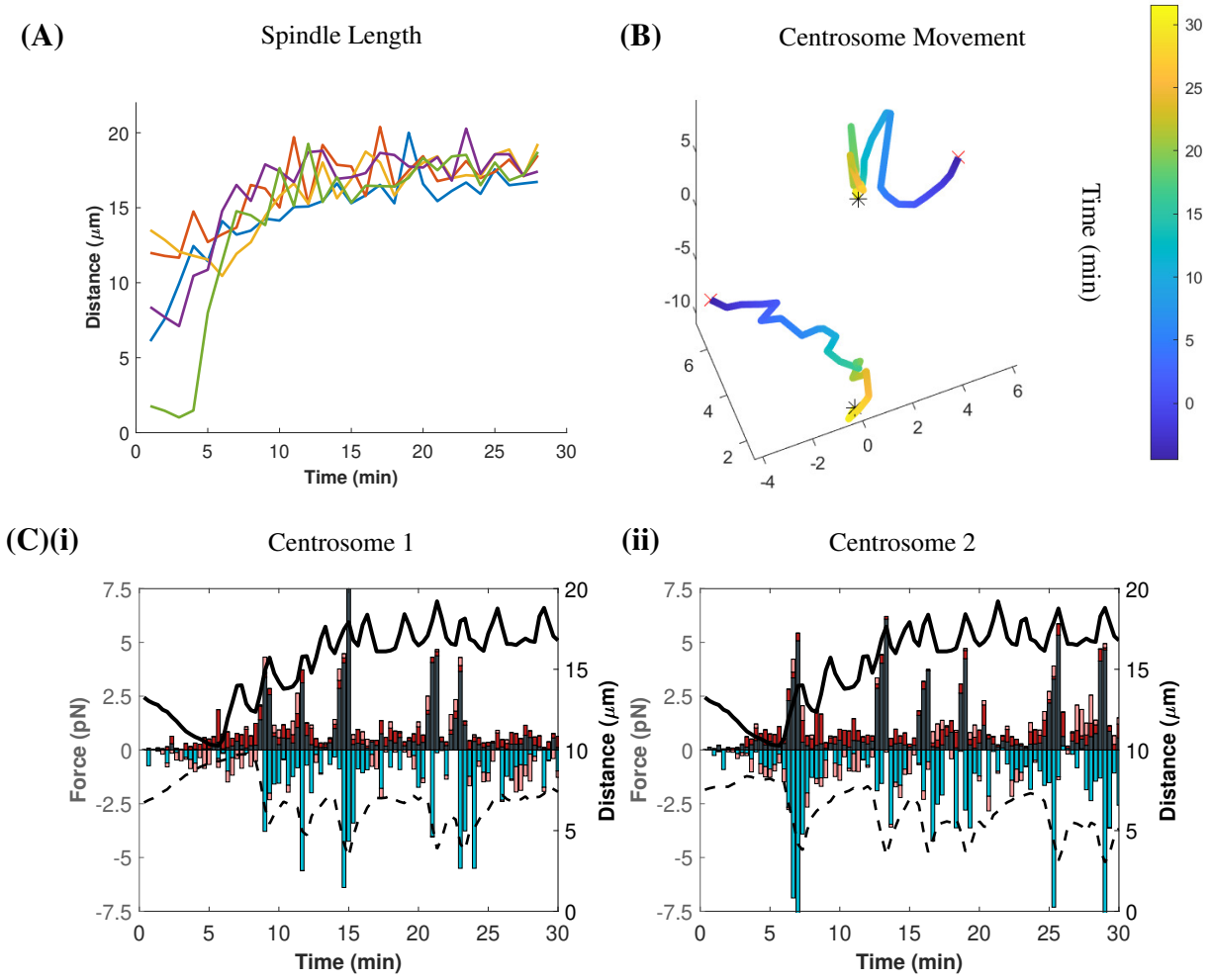

Figure S3: **Bipolar spindle formation and cortical dynein-driven oscillations in spindle length extend to three-dimensions.** (A) Spindle length over time is shown for 5 simulations. (B) Plot of centrosome movement over time for the simulation in Movie M8. Each line is a centrosome, red 'x' is initial centrosome position, black asterisk is final centrosome position. (C) Representative images of force components over time for centrosome "1" (i) and centrosome "2" (ii) from a single simulation, overlaid with spindle length (solid black line) and the minimal centrosome distance to the cell cortex (dashed black line).

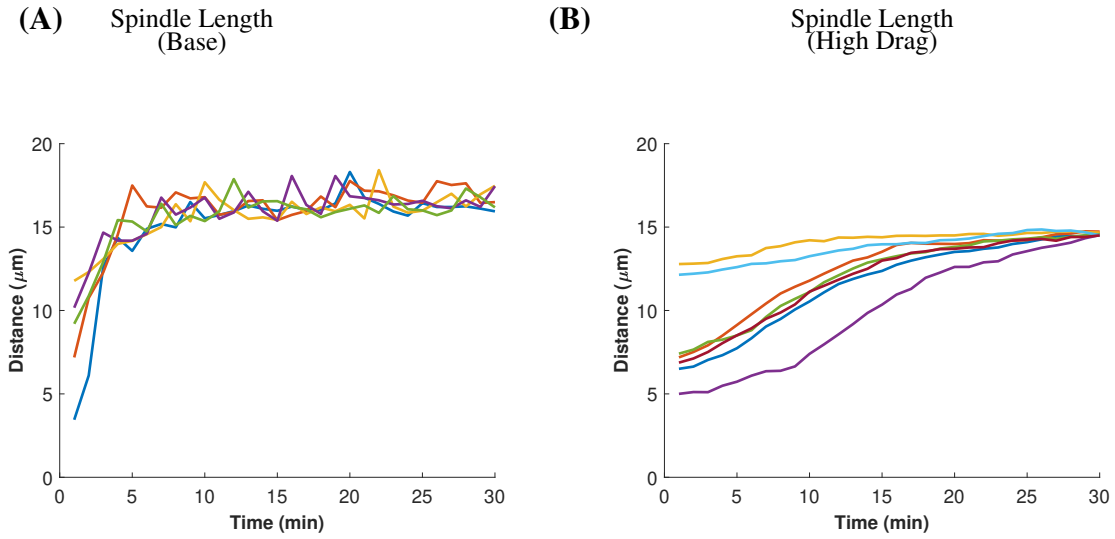

Figure S4: **Increasing the drag coefficient alters the dynamics of bipolar spindle formation.** Curves of spindle length over time for the base case (A) and the high drag case (B). High drag is defined as 5ξ. Individual traces are shown for 6 simulations.

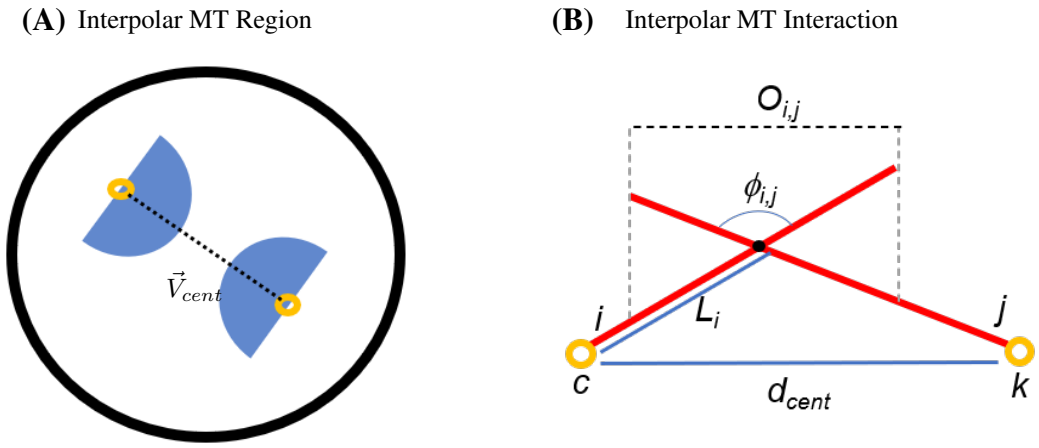

Figure S5: **Interpolar MTs.** (A) Schematic of interpolar MT region. Black dashed line indicates the vector between the centrosomes ($\vec{V}_{cent}$). Interpolar MTs are those that lie within the blue shaded regions. (B) Schematic of interpolar MT interaction. MTs i, j are nucleated from centrosomes c, k, respectively.

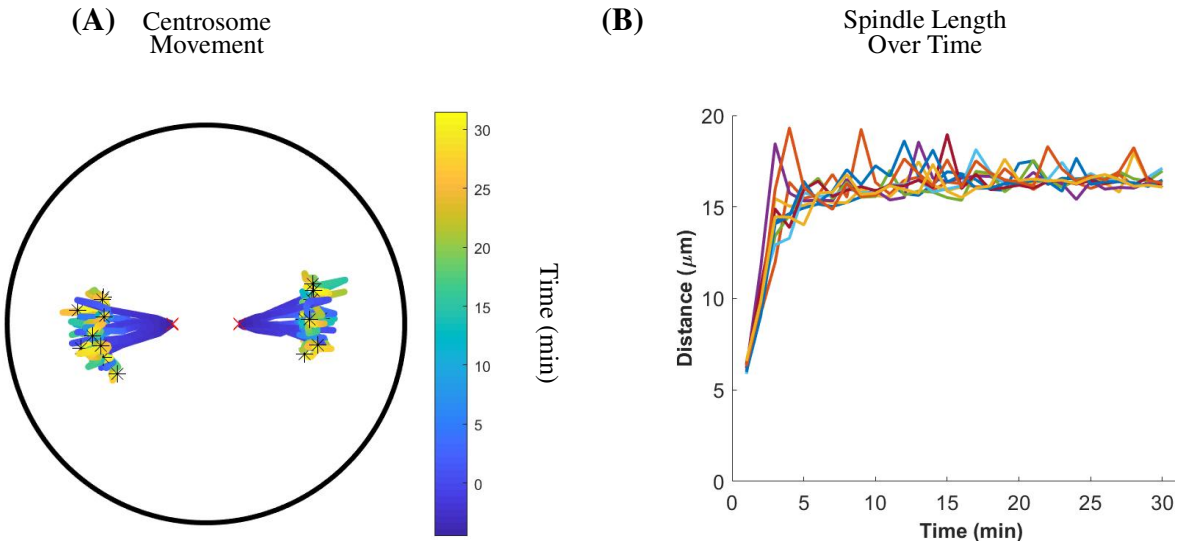

Figure S6: **Multiple simulations with the same initial centrosome positioning reveal variations due to model stochasticity.** (A) Centrosome movement traces over time for 10 simulations with the same initial centrosome positions. Red 'x' is initial position, black asterisk is final position. (B) Traces of spindle length over time for 10 simulations with the same initial centrosome positions. Each line is a simulation.

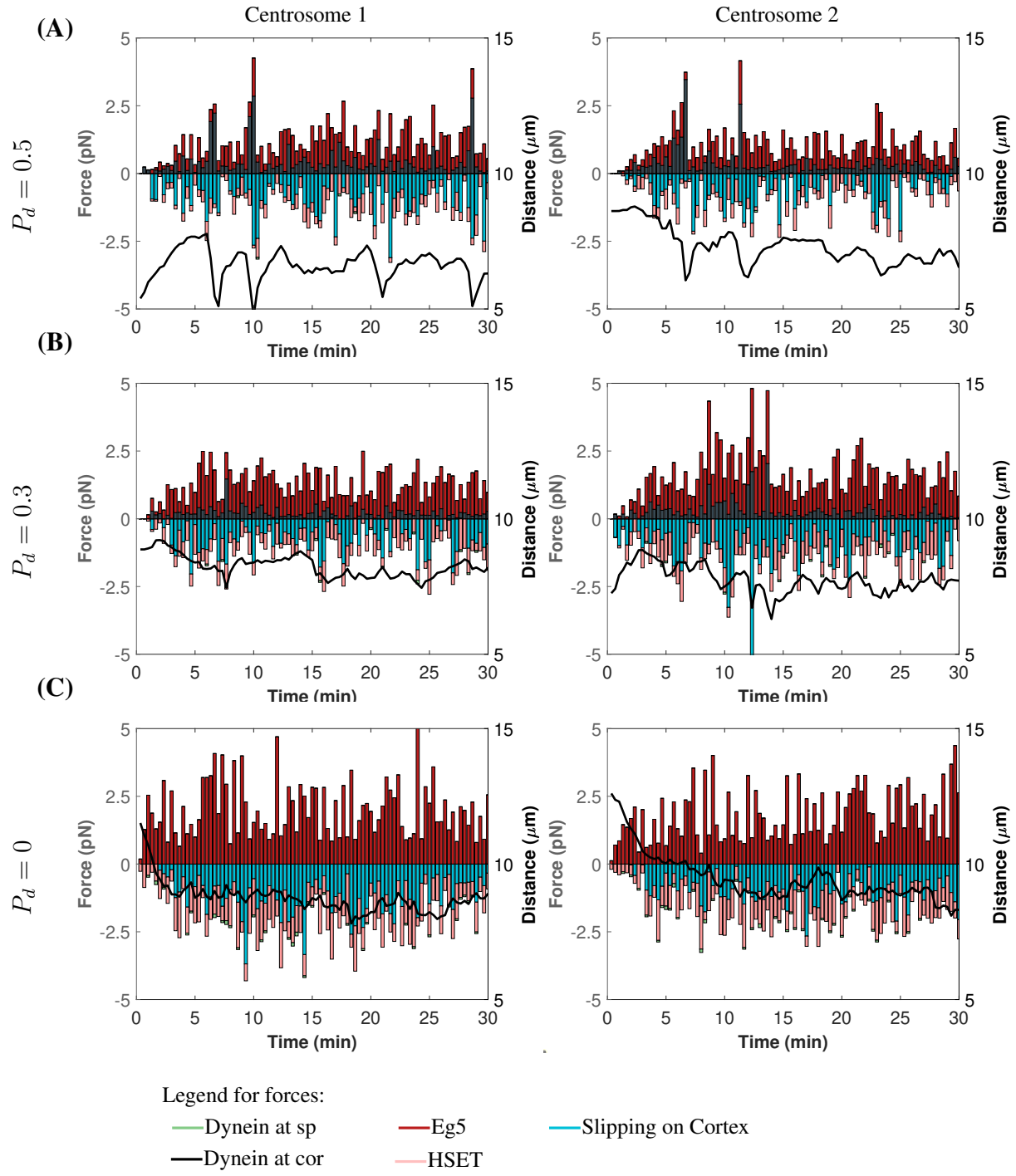

Figure S7: **Reduction and loss of cortical dynein impacts centrosome distance to the cell cortex.** Representative images of force components over time for a single simulation with $P_d = 0.5$ (A), $P_d = 0.3$ (B), $P_d = 0$ (C), overlaid with the minimal centrosome distance to the cell cortex (black line). A positive force is one that pushes centrosomes apart while a negative force is one that pulls centrosomes together. The left column is centrosome "1" and the right column is centrosome "2" from the same simulation.